Weather and Climate Extremes 43 (2024) 100638

Contents lists available at ScienceDirect

Weather and Climate Extremes

journal homepage: www.elsevier.com/locate/wace

Saharan rainfall climatology and its relationship with surface cyclones

Moshe Armon [a,*], Andries Jan de Vries [b], Francesco Marra [c,d], Nadav Peleg [b], Heini Wernli [a]

[a] Institute for Atmospheric and Climate Science, ETH Zurich, 8092 Zurich, Switzerland
[b] Institute of Earth Surface Dynamics, University of Lausanne, Lausanne, Switzerland
[c] Department of Geosciences, University of Padova, Padova, Italy
[d] Institute of Atmospheric Sciences and Climate, National Research Council of Italy (CNR-ISAC), Bologna, Italy

ARTICLE INFO

Dataset link: https://doi.org/10.5281/zenodo.10074760

Keywords:
Desert precipitation
Heavy precipitation events
IMERG
Surface cyclones
Sahara

ABSTRACT

The Sahara is the largest and driest of the hot deserts on Earth, with regions where rainfall reaches the surface on average less than once a year. Water resources are scarce, and rainfall tends to occur sporadically in space and time. While rain is a precious resource in the Sahara, heavy precipitation events (HPEs) in the desert have the potential to trigger flash floods on the barren soil. Because of the sparse rainfall monitoring network and the relatively poor performance of global models in representing rainfall over the Sahara, the analysis of Saharan HPEs has primarily relied on case studies. Therefore, general rainfall characteristics of Saharan HPEs are unexplored, and the prevailing weather conditions enabling such rainfall are unknown. To tackle this problem, we utilised satellite-derived precipitation estimations (IMERG) spanning 21 years (2000–2021) to identify $\sim 42 \cdot 10^3$ small ($>10^3$ km^2) to large ($<10^6$ km^2) HPEs in the Sahara and to extract their rainfall properties, and atmospheric reanalyses (ERA5) to examine the corresponding meteorological conditions in which they develop. Three case studies illustrate the relevance of cyclones for exceptionally large HPEs, including one in the driest region of the Sahara. Saharan HPEs occur, on average, every second day. They are more common in summer than in the other seasons, occur most frequently in the southern Sahara, and exhibit a clear convectively-driven diurnal cycle. Winter events have, on average, larger spatial extent, longer duration, and are characterised by larger areas exhibiting more extreme rainfall in terms of return periods. Autumn HPEs are concentrated in the western Sahara, while events in the north of the desert and in its driest core in the northeast occur mainly in winter and spring. In these regions, north of the Tropic of Cancer, events are highly associated with surface cyclones. HPEs that were associated with cyclones are characterised by larger spatial extent and rainfall volume. Considering that weather and climate models often depict synoptic-scale weather systems more accurately than rainfall patterns, the association of Saharan HPEs with surface cyclones and other synoptic-scale systems can aid in comprehending the effects of climate change in the desert. Furthermore, it underscores the potential for higher predictability of these events.

1. Introduction

A fifth of the world's population lives in arid and semi-arid areas. The low amount and sparse occurrence of precipitation in desert regions makes the rare rainstorms occurring there most treasured for human life and for a variety of ecosystems in these regions (e.g., D'Odorico and Bhattachan, 2012). At the same time, these rainstorms pose a danger to desert communities, as they can trigger natural hazards (Yin et al., 2023); in the driest deserts, rainfall accumulations as little as a few millimetres can yield flash floods and a few tens of millimetres can even trigger debris flows (Tooth, 2000; Zoccatelli et al., 2019; Shmilovitz et al., 2020; Rinat et al., 2021; Siman-Tov and Marra, 2022).

The largest of all hot deserts, the Sahara ($\sim 9\times10^6$ km^2; Tucker et al., 1991), is considered to be the driest place on earth (Kelley, 2014). However, rainfall, and particularly heavy precipitation events (HPEs), are reported in the Sahara from time to time, mainly as sporadic anecdotes (e.g., Clarke, 1973; Pedgley, 1974; Fink and Knippertz, 2003), or when devastating floods occur (badawy Moawad et al., 2016). Nevertheless, a large portion of the Sahara is so deserted that even the most intense storms often pass by unnoticed, and are regarded only when using post-event proxies (Schepanski et al., 2012). Another occasion in which events are noticed, is when storms traverse into or out of the Sahara and pass over the more populated desert outskirts. A devastating example is Storm Daniel, a Mediterranean cyclone that hit the coast

* Corresponding author.
E-mail address: moshe.armon@env.ethz.ch (M. Armon).

https://doi.org/10.1016/j.wace.2023.100638
Received 21 June 2023; Received in revised form 8 November 2023; Accepted 12 December 2023
Available online 14 December 2023

of Libya on 10 September 2023 on its way to the northern Sahara. The storm triggered major floods in northern Libya, affected the lives of $\sim 250\,k$ people and left behind more than 4300 casualties (OCHA, 2023), as well as unusual floods in the Libyan Desert (northern Sahara; Copernicus, 2023).

Reliable observations of HPEs are essential for (a) a better understanding of rainstorm characteristics and the atmospheric dynamics in such environments; (b) providing early warning for natural hazards; and (c) coping with present and adapting to future implications of such storms. Current projections show that while deserts might be expanding (e.g., Huang et al., 2017; Wang et al., 2021), the population in deserts may grow by at least a few hundred million people, in particular in the Sahara (Huang et al., 2016; Lickley and Solomon, 2018). However, if it is not known when and where rain precipitates, and how much of it reaches the ground, it is almost impossible to infer what are the atmospheric processes that bring about HPEs.

Heavy rainfall in deserts – and precipitation in general – occurs at small spatiotemporal scales over discrete events (Sun et al., 2006; Li et al., 2023), which can often be associated with specific synoptic-scale patterns (e.g., Maddox et al., 1980; Pook et al., 2014; Dayan et al., 2015; Armon et al., 2018). The African Monsoon and the Saharan heat low are often associated with Saharan precipitation, mainly at the desert's southern fringe, and during summer (e.g., Parker et al., 2005; Lavaysse et al., 2010; Funk et al., 2016). However, a few case studies described HPEs occurring in winter or transition seasons, in the northern parts of the desert, usually in association with a surface cyclone (e.g., Fink and Knippertz, 2003; Saidi et al., 2020, and also the abovementioned Storm Daniel). Whereas case studies provide insight into the general processes, they are not necessarily representative of the entire population. Our understanding of HPEs in deserts is still far from being complete (Mirzabaev et al., 2019). As far as we know, no scientific research has investigated the climatological aspects of HPEs in the Sahara. More so, because of its dryness, analyses of HPEs in the inner and driest part of the Sahara are almost absent from the literature. In such hyper-arid regions, nearly all rain events are HPEs by definition. Citing local knowledge, Bagnold (1990, p. 136) in his visit to the region, claimed that in the core of the Sahara "the last effective rain had fallen some seventy years before". Can rainfall occurrence indeed be so low? If it rains only once every many decades, which atmospheric processes bring this about, and how much rainfall reaches the surface? Could it be that heavy rainfall occurs more frequently, but no one witnesses it? To answer such questions, we rely on remote-sensing data to reveal when and where HPEs occur in the Sahara and what their magnitude and characteristics are. In addition, we quantify the co-occurrence of surface cyclones with HPEs, and to this end use atmospheric reanalysis data. The following subsections provide more detailed information about the atmospheric controls on rainfall in the Sahara, the relation between cyclones and precipitation in the Sahara, and the challenges that come with observations of rainfall in the desert.

1.1. Atmospheric controls on absence and sparse occurrence of Saharan rainfall

The aridity of the Sahara stems from a variety of large-scale atmospheric factors that promote subsidence, low-level divergence, and thermal stability. These factors, interconnected to one another, include (a) the Hadley cell's poleward subsiding branch (Ziv et al., 2004); (b) the Sahara-Azores subtropical high (e.g., Chauvin et al., 2010); (c) ageostrophic flow of the tropical easterly jet that strengthens subsidence at its right-exit region (Webster and Fasullo, 2003); (d) the monsoon-desert mechanism related to remote diabatic heating over the Asian monsoon (Rodwell and Hoskins, 1996, 2001); (e) the eastern subsiding branch of the Walker cell at the northeast of the desert (Dayan et al., 2017); and (f) the cool waters of the Canary Current west of the Western Sahara combined with the trade inversion, which inhibits the ascent of low-level air parcels (Nicholson, 2011, p. 399).

The vast extent of the Sahara makes it possible for rain to be associated with both mid-latitude rain-bearing systems and tropical-origin systems (e.g., Morin et al., 2020). In addition, tropical-extratropical interactions may play a significant role in Saharan precipitation (Knippertz, 2005; de Vries, 2021). Previous studies have predominantly focused on either the periphery of the Sahara or nearby regions, leaving the synoptic-scale systems that contribute to rainfall over the vast desert relatively speculative. For example, precipitation in the southern Sahara is mainly associated with northward intrusions of summertime monsoonal lows, tropical easterly waves, and convection related to orographic lifting and surface heating in the vicinity of the Saharan heat low (Parker et al., 2005; Mekonnen et al., 2006; Lavaysse et al., 2009, 2010; Engelstaedter et al., 2015; Hurley and Boos, 2015; Funk et al., 2016; Nicholson, 2018). In contrast, the northern and western Sahara is influenced by autumn to wintertime southward deflected extratropical cyclones originating from the North Atlantic and the Mediterranean (e.g., El-Fandy, 1946; Alpert and Shay-EL, 1994), Sharav Cyclones originating at the lee of the Atlas Mountains mainly in spring (Alpert and Ziv, 1989; Hannachi et al., 2011), tropical moisture exports in the form of Tropical Plumes (e.g., Knippertz et al., 2003; Rubin et al., 2007; Skinner and Poulsen, 2016), and quasi-geostrophic lifting associated with warm conveyor belts (Chaqdid et al., 2023). In the eastern Sahara, known weather phenomena include the active Red Sea Trough (Ashbel, 1938; Krichak et al., 1997; Awad and Almazroui, 2016) and Tropical Plumes (also termed Sudanese Tracks/Currents in the Arabian Peninsula), active in all seasons except for the summer (Barth and Steinkohl, 2004; Tubi et al., 2017). However, to obtain a comprehensive understanding of the synoptic-scale weather systems that can lead to the formation of HPEs in the Sahara, it is necessary to first identify HPEs and their properties, including their location, timing, spatial extent, and magnitude.

1.2. Heavy precipitation events and surface cyclones in the Sahara

A key synoptic-scale weather system that plays a significant role in inducing heavy precipitation across multiple regions globally is surface cyclones (Pfahl and Wernli, 2012). Saharan cyclogenesis tends to occur in the lee of the Atlas Mountains. These cyclones progress across the desert and may lead to substantial precipitation and other severe phenomena such as dust storms (e.g., Campins et al., 2011; Russo et al., 2020). Interestingly, an upward trend in the frequency of Saharan cyclones in autumn and a downward trend in summer was found by Ammar et al. (2014). Naturally, cyclones vary across the Sahara and with seasons in terms of the dynamical forcing of their genesis and intensification, and their relationship with heavy precipitation.

During summer, the Saharan heat low is quasi-permanent and extends between the Atlas and Ahaggar Mountains (Fig. 1) on the western side of the Sahara (Schepanski et al., 2017). When the low is anomalously deep, it is associated with convective updrafts and rainfall with a clear diurnal cycle (e.g., Lavaysse et al., 2010). This precipitation is primarily observed over the low's southern part – the Sahel – and not in its northern side, where upper-level subsidence dominates (Nicholson, 2009). In the other seasons, cyclones are more of a transient phenomenon, with Mediterranean (and Atlantic) cyclones passing to the north and west of the Sahara (Wernli and Schwierz, 2006; Campins et al., 2011; Hannachi et al., 2011; Ammar et al., 2014). It has been acknowledged for quite some time that these cyclones are relevant for peak precipitation in autumn in the northwestern Sahara, and winter in the northern Sahara (Griffiths and Soliman, 1972; Fröhlich et al., 2013; Morin et al., 2020). However, since rainfall events are not well observed in the Sahara, the relative contribution of these cyclones to Saharan rainfall is unknown. In particular, since only a few events were recorded at the core of the Sahara, the contribution of cyclones to rainfall in the core of the Sahara is unclear.

Common to all seasons and regions in the Sahara, is that rainfall tends to occur in short-duration and localised events. HPEs make an

important contribution to total precipitation and are the most impactful in terms of natural hazards and in replenishing water resources (e.g., Milewski et al., 2009). Total rainfall in such events may be much more than monthly averages, and even the annual average rainfall. For example, rainfall in Biskra, Algeria, in just two days in September 1969 summed to 299 mm, roughly twice the annual average and 17 times the monthly average (Nicholson, 2011, p. 425). Can we generalise such events? Do these events share any common characteristics or patterns?

1.3. Rainfall observations in the Sahara

Given that desert rainfall is characterised by more confined spatiotemporal scales compared to rain in other regions (e.g., Sharon, 1972; Wasko et al., 2016; Peleg et al., 2018) and since in-situ rainfall observations in the Sahara are so scarce (Kidd et al., 2017), it is difficult to provide answers to these questions. Using 19-year satellite-based daily quantitative precipitation estimations (QPEs), Morin et al. (2020) explored this rainfall localisation. They found that rainfall in the hyperarid parts of the Sahara is roughly three to six times more spatially confined compared to rainfall in semi-arid regions. This localisation was manifested by the small area exhibiting rainfall during rainy days: over the arid area they examined, on average, only 4% of the area exhibited rainfall. In 2020, the average spatial density of daily rain gauges reporting to the Global Historical Climatology Network (GHCN) in the Sahara was $\sim 1:200{,}000\,\mathrm{km}^2$ (Fig. 1). This means that in fact, rain gauges are orders of magnitude too sparse to represent Saharan rainfall. Sub-daily gauge measurements, needed for analyses of local scale HPEs, are presumably even scarcer. The same holds for weather radars, with close to zero radar coverage over the Sahara (Heistermann et al., 2013; Saltikoff et al., 2019). Satellite-based QPEs are therefore practically the only available observation-based source of information to assess precipitation at sub-daily resolutions and are increasingly used for the Sahara (Harada et al., 2003; Kelley, 2014; Marra et al., 2022b).

In most populated areas, large-scale validation of satellite-based QPEs is carried out using rain gauges. Clearly, this does not apply to the Sahara. As indicated by Beck et al. (2017), gauge-corrected precipitation data have their largest uncertainty over arid regions, where their performance is worse compared to other climate zones. Therefore, no long-term wide-extent validation of satellite products was previously carried out in the Sahara. However, we may still gain insight into the validity of satellite QPEs from (a) case study validations from the Sahara or longer-term studies from nearby regions; (b) large-scale analyses in which the Sahara is included, even if it accounts for only a small portion of the analysis; and, (c) comparison with results from numerical modelling. Validation examples of this are given in Section 2.

In contrast to most satellite QPEs, atmospheric reanalyses generally do not assimilate direct precipitation observations. Therefore, precipitation fields from reanalysis products rely essentially on the underlying numerical model. Nevertheless, they may be useful in observation-scarce regions. However, it seems that over arid regions reanalysis-based rain fields are inferior compared to other regions (Beck et al., 2017), and were found to not represent well rainfall variability e.g., in the arid and semi-arid highlands of Yemen (Al-Falahi et al., 2020), nor local-scale high-intensity rainfall in the eastern Mediterranean deserts (Armon et al., 2020; Rinat et al., 2021). Indeed, without the explicit representation of convective processes, model-based rainfall cannot be expected to represent precipitation with high reliability, even if the larger-scale meteorological environment is well-represented (e.g. Prein et al., 2015). Given the lack of ground-based observations, however, reanalyses can provide an independent estimate from the satellite products, as well as information on the atmospheric processes at synoptic scales that are responsible for the formation of rain events.

Based on this brief literature overview of the atmospheric controls on the Saharan hydroclimate, the inherent challenges of precipitation observations in these regions, and the main research gaps, we formulate the three main objectives of this study. First, to identify and characterise HPEs in the Sahara in terms of their spatial distribution and extent, frequency, timing (i.e., seasonality, diurnal pattern), duration, magnitude (rainfall volume and depth), and extremeness levels. The second objective is to examine the relationship between HPEs and surface cyclones. In our analysis, we focus primarily on non-summer events and the dry "core" of the Sahara. Lastly, we aim to provide a comprehensive list of HPEs that have occurred between June 2000 and May 2021 that may be useful for studies of HPE impacts in the Sahara.

2. Study area and data

The Sahara's exact extent is somewhat ambiguous (e.g., Warner, 2004, Chap. 3). It extends from a few tens to hundreds of kilometres south of the Mediterranean coast to 1500 km south toward the Sahel, and from the Atlantic Ocean in the west to the Red Sea in the east (Fig. 1). Its southern edge was determined by Tucker et al. (1991) to be a gradual shift to steppe vegetation characterising the Sahel, where higher mean precipitation occurs. Here we adopt a "public domain" delineation of the Sahara (Kelso and Patterson, 2010), which is mainly in agreement with Tucker's Sahara outline. This definition is easily reproducible, and slight variations of it are not expected to substantially alter the results of this study. It is important to note that based on this delineation, the Sahara boundary crosses aridity index isolines (Fig. 1). However, since most aridity indices are based on "nearly non-observable" precipitation, the most appropriate aridity index used in determining the Sahara's extent is arguable. The dry "core" of the Sahara is defined here as the spatially continuous region where mean annual precipitation does not exceed 15 mm according to satellite QPE (see below; Fig. 1, red contour).

The Sahara is sheltered from low-level airflow across its northwestern edge by the $\sim$ 4000 m high Atlas Mountains, in the east by the $<$ 2000 m Red Sea Hills (or Itbay Mountains) and in the southeast by the Ethiopian Highlands ($\sim$4500 m) and the Marrah Mountains ($\sim$3000 m). In the interior of the desert lie two other major mountain ranges, the Ahaggar and the Tibesti, and expansive plains. Most of the land is barren, covered by rock outcrops and younger sedimentary units including $\sim$ 15% of sand surfaces. Within this vast area ($\sim 10.6\times10^6$ km^2) lies perhaps the driest place on earth (Kelley, 2014). Other regions, mainly at the verge of the Sahel in the southern Sahara, are much wetter. In general, however, evaporation greatly exceeds precipitation throughout the region we consider here as the Sahara (Fig. 1).

The study uses the following two datasets for a period of 21 years (June 2000 until May 2021): (a) QPEs are derived from the Integrated Multi-satellitE Retrievals for the Global Precipitation Measurement (GPM; Hou et al., 2014) mission (IMERG; Huffman et al., 2020). These data (IMERG V06B-final; Huffman et al., 2019), at a 0.1° spatial resolution, are based on a sophisticated incorporation and intercalibration process of satellite-based active and passive microwave, and IR retrievals, which are then adjusted with ground-based gridded precipitation data. Daily-aggregated data (00:00 UTC to 23:59 UTC) are used for identifying HPEs, and 30-minute data are used for the characterisation of these HPEs (as explained in the next section); and (b) meteorological fields, at 0.5°, 60 min resolution, for the same period, are extracted from the European Centre for Medium-Range Weather Forecasts (ECMWF) ERA5 reanalysis (Hersbach et al., 2020). ERA5 reanalysis is based on state-of-the-art hybrid incremental 4D-Var data assimilation, which is the same as the one used in the ECMWF operational weather prediction system in 2016 (IFS cycle 41r2). Data assimilated into the reanalysis include observations from in-situ ground stations, upper air balloons and aircraft, satellites, inter alia. Like rainfall observations, in-situ meteorological measurements in the Sahara are scarce as well. However, it is important to note that satellite measurements have a similar density over the Sahara as in other regions of the world. A comparison of mean annual precipitation in ERA5 and IMERG is shown in Fig. A1.

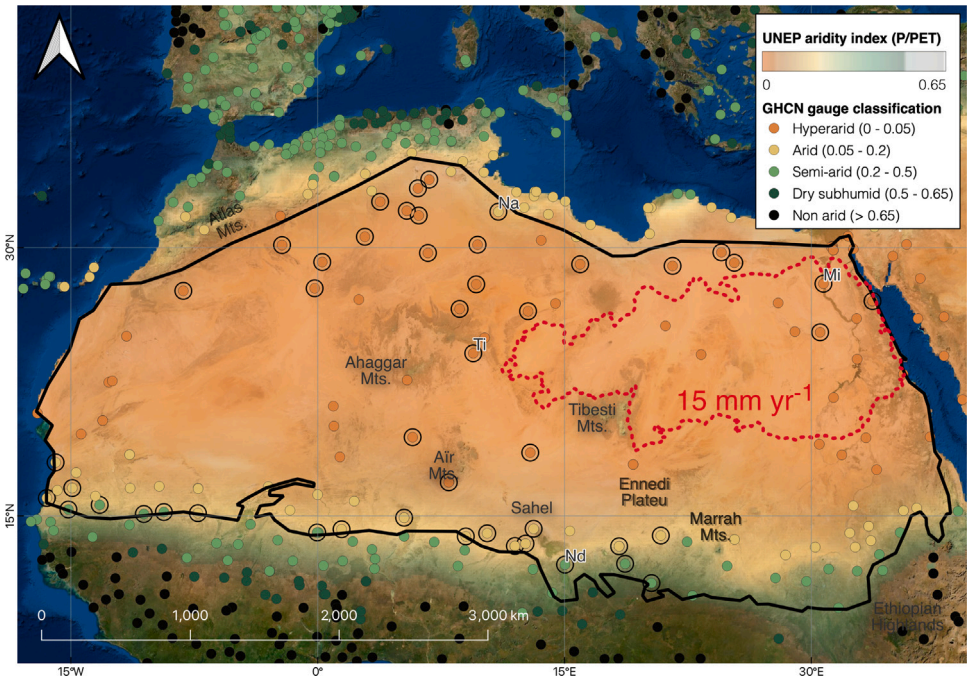

Fig. 1. Study area (outlined in black) and the dry core of the Sahara (red), where mean annual precipitation (IMERG-based) is ≤ 15 mm. Circles represent daily GHCN gauges (Menne et al., 2012) in the vicinity of the Sahara. Saharan gauges that operated in 2020 are marked with black circles. Four gauges used for comparison of return periods (Fig. A4) are marked: Na = Nalut, Libya, Ti = Tiska, Algeria, Nd = N'Djamena, Chad, Mi = Minya, Egypt. Colours represent the UNEP (1992) aridity index (precipitation divided by potential evapotranspiration) calculated from the CRU TS v. 4.05 dataset (Harris et al., 2020). (For interpretation of the references to colour in this figure legend, the reader is referred to the web version of this article.)

The reliability of IMERG QPEs in deserts was evaluated in several studies. For example, Dezfuli et al. (2017) assessed the validity of IMERG-GPM over Africa and compared it with other global QPE products. Their study indicated that IMERG performs better compared to other available datasets, although differences between different products were greatest over the high topography of the north-western Sahara. Similarly, Morsy et al. (2021) showed good overall performance of IMERG when comparing it to gauge data in the Sinai desert, and Mahmoud et al. (2021) reached the same conclusion when examining IMERG over Saudi Arabia. Validation results point to worse performance in complex-topography arid regions, with the best overall performance of the "final" version of IMERG compared to other, non-gauge corrected versions of the dataset in both the Moroccan drylands and Arabia, although on the days with the heaviest precipitation non-corrected versions of IMERG sometimes outperform IMERG-final (Mahmoud et al., 2021; Li et al., 2021; Rachdane et al., 2022). While biases may increase with aridity (Milewski et al., 2015), large-extent validation in Australia, including the Australian interior deserts, showed that IMERG performs quite well in terms of bias, correlation, and structural similarity (Islam et al., 2020). Satellite QPEs can overestimate the intensity of rainfall over deserts due to sub-cloud evaporation (Dinku et al., 2011); however, in most cases, they still provide valuable information about rain and no rain conditions, as well as the extent of precipitation events in space, and even their magnitude.

3. Methods

3.1. Identification of HPEs

A pixel-based climatology is used to identify locally-substantial HPEs in the IMERG precipitation dataset (Armon et al., 2020). To facilitate computational efforts, events were identified using the daily version of IMERG, but properties of every event were then extracted using the 30 min version of the data. To avoid contamination from weak precipitation or noise due to the difficulty in retrieving precipitation over desert soils, we only used time steps when precipitation was greater than 1 mm d^{-1}. We set the 90th percentile of this conditional rainfall as an *intensity threshold* for heavy precipitation at every pixel (Fig. 2a), and defined events where this threshold was exceeded over spatially connected regions of at least 1000 km^2 (roughly 10 connected pixels, note definition below). This *spatial threshold* was defined low enough to enable the representation of small-scale HPEs that can still be meaningful at the local and regional levels, e.g., in triggering flash floods (Zoccatelli et al., 2019), but large enough to exclude spurious values at single pixels. This procedure resulted in the identification of HPEs throughout the Sahara (Fig. 2b). We also tested 10,000 and 25,000 km^2 as spatial thresholds, which yielded similar results with an almost identical spatial distribution, but a decrease in the frequency of events (Fig. A2). To overcome the rigid, and somewhat arbitrary values of the selected thresholds and to account for precipitation in close-by regions fluctuating above and below the threshold, we considered pixels to be spatially connected not only when they neighbour one another but also when they are not more than $\sqrt{A}$ km apart, where A is the spatial threshold. In our case $A = 1000$ km and therefore the buffer is ~ 3 IMERG pixels (respective distances were used for the other tested spatial thresholds), similar to the minimal possible radius for events with a spatial threshold of 1000 km^2. We examined also a twofold and a threefold increase in this buffer region, with no substantial change in the total number of events. A decrease of the buffer region is not desired, as well as a decrease in the spatial threshold, since it gets too close to the data resolution. It must be noted, however, that events that are particularly localised, i.e., < 1000 km^2 are excluded from our analysis. Events identified over sequential daily time steps are considered the same event if their edges are not more than twice the buffer size apart from one another, thus allowing for events to have a duration greater than one day. Lastly, events were only identified over the study region, meaning that events occurring on the border of the Sahara were truncated.

3.2. Properties of HPEs

For each of the identified HPEs, we extracted several properties from the high-resolution (30 min) IMERG dataset. Since events were

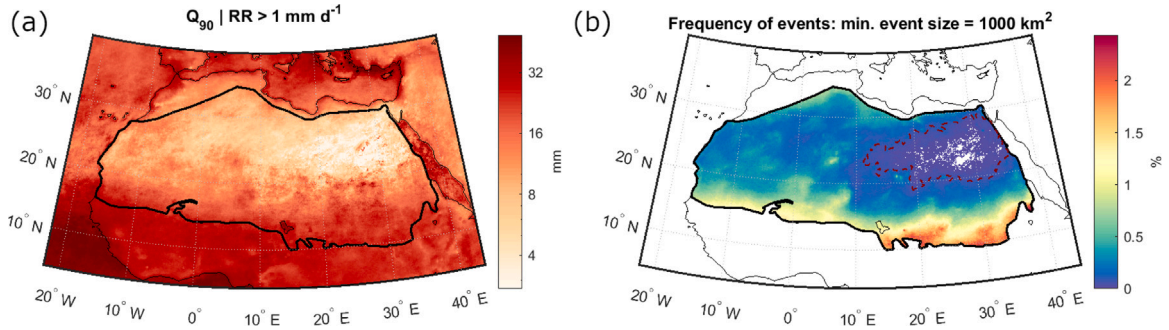

Fig. 2. Climatological properties in identifying HPEs. (a) 90th percentile of daily intensities for wet (>1 mm d^{-1}) days. (b) Frequency of HPEs during the study period (Section 3.2), where the spatial threshold defining the minimum event area is set to 1000 km^2. Frequencies of HPEs using larger spatial thresholds are in Fig. A2 and the season-specific frequency is in Fig. A3. (For interpretation of the references to colour in this figure legend, the reader is referred to the web version of this article.)

identified on a daily basis, rainfall can in principle start before or end after the identified HPE. Therefore, rain properties were extracted over all pixels that are associated with the HPE starting 12 h before the beginning of the HPE and ending 12 h after its marked finish. The following properties are extracted for every HPE:

1. Mean rain depth (in mm). That is the spatially averaged accumulated precipitation over all pixels associated with the HPE.
2. Volume of rainfall (km^3).
3. Rainfall duration (h). This was determined as the shortest duration during the event over which 90% of the rainfall volume was precipitated.
4. HPE area (km^2). The size of the area that was identified as a HPE.
5. Area of extreme precipitation (km^2). The size of the area over which daily rain intensities exceeded the 2-y, 10-y and 100-y return periods for a one-day duration (Section 3.4). For events longer than one day, we used only the day with the largest rainfall volume.

Additionally, the diurnal cycle of precipitation intensity during HPEs was calculated based on precipitation over the identified HPEs, and the relative contribution of HPEs to total precipitation was calculated for the whole domain.

3.3. Climate composites and anomalies

A set of meteorological fields from the ERA5 dataset were used to define the anomalous conditions during HPEs compared to climatology. These are geopotential height, sea level pressure (SLP), winds at different pressure levels, near-surface (2 m) temperature, total column water (TCW), and potential vorticity (PV). Since events were identified on a daily basis, we used a single reanalysis time step to represent the conditions during each event. To represent the conditions at or just before most convective storms, this was set to 14:00 UTC (mostly 3 or 4 pm local time, depending on the location). Composites were calculated as the mean of all values during HPE days, and anomalies were computed as the difference between the mean climate conditions for the season and the mean HPE conditions. Normalised anomalies were derived by dividing the anomaly by the climatological standard deviation of the same parameter. To overcome biases related to intra-season differences in the number of identified HPEs (e.g., a greater number of events at the beginning of a season), we corrected the above-mentioned composite anomalies with this frequency bias serving as a weight for the seasonal averaging. Therefore, both mean values and standard deviations were first calculated on a monthly basis and then the weighted sum was calculated.

3.4. The degree of extremeness of the HPEs

To quantify the extremeness level of HPEs (Section 3.2: item 5), we extracted the intensity values corresponding to 2–100 y return periods. The small number of rainy days per year and the length of the precipitation record limit the applicability of traditional extreme value analyses to assess the extremity of the identified HPEs. Therefore, we utilised a non-asymptotic approach, which considers a large portion of the record rather than just the annual maxima (Zorzetto et al., 2016). This approach, termed Simplified Metastatistical Extreme Value (SMEV), was proven beneficial for relatively short records and for regions with a small number of events per year (Marra et al., 2019). We applied the method to the IMERG daily data. The parameters used are based on an application of the SMEV to the entire African continent using satellite-based precipitation estimations (Marra et al., 2022b). These include the upper quartile of the data as defining the stretched-exponential right tail, one day as the separation distance between two consecutive ordinary events (see also Marra et al., 2020). In addition, we used 1 mm d^{-1} threshold as an indication for "rainy days". As an example for the SMEV application, the intensity-frequency curves over four different gauges in varying degrees of aridity across the Sahara (Fig. 1) are given in Fig. A4a,b for satellite-derived data, and for rain gauge-based data, respectively.

3.5. Cyclone detection and attribution

To identify the relation between cyclones and HPEs we used binary cyclone mask fields derived from analyses of global ERA5 SLP maps (Sprenger et al., 2017). Cyclones are defined as enclosed regions containing one or more SLP minima (Wernli and Schwierz, 2006). For every HPE we searched for the closest cyclone mask, on a 6-hourly basis, meaning that for each HPE day, we would find up to four cyclone masks (Fig. A5). These can arise either from the temporal progression of cyclones or from the genesis and lysis of individual cyclones passing by the HPE. The closest distance throughout the duration of the HPE, calculated from the edge of the cyclone mask to the edge of the corresponding HPE, is then considered the distance of the HPE from a cyclone (Fig. A5b). If this distance is 0, i.e., the cyclone mask and the HPE overlap for at least one of the 4-daily cyclone masks, the HPE was attributed to the cyclone.

Still, other HPEs, for which there is no spatial overlap between a cyclone and the HPE, can possibly be associated with cyclones. To attribute such HPEs to cyclones we performed a Monte Carlo simulation in which, for every HPE we choose a "false" cyclone sample of 100 random dates from the entire study period through the year. Using this procedure we were able to test the minimum distance required to attribute a HPE to a cyclone. Our null hypothesis (H_0) is that the event cannot be associated with a cyclone, and the alternative hypothesis is that we cannot rule out its association. We define $\alpha = 5\%$, and therefore

for each HPE we find the 5th quantile of the closest distances of the random cyclones. Performing this iteratively over all the identified HPEs and taking the median result yielded a separation distance of 180 km (Fig. A6). When the closest distance between a HPE and a cyclone is larger than that, we considered HPEs as not being associated with cyclones. Given that in this procedure we choose cyclones from randomly selected dates, and not e.g., only from dates with no rainfall, the estimate of the separation distance may be considered a conservative estimate. Thus, more cyclones are potentially associated with HPEs, however, we ensure a lower false association ratio. Additionally, to discern whether the examined properties (Section 3.2) are different between HPEs associated and non-associated with cyclones, we used the Mann–Whitney test with $\alpha = 5\%$.

4. Case studies

We first present three case studies of especially large-area HPEs that are associated with cyclones. The first (Section 4.1) occurred in autumn in the northwestern Sahara, and is chosen to demonstrate the potential of an extratropical cyclone to produce tremendous amounts of precipitation in the Sahara. The second case study (Section 4.2) is a summer event in the southeastern Sahara, and is an example of a rain event occurring outside of the "classical" monsoon regions, highlighting the connections between Saharan and non-Saharan precipitation events. The third case study (Section 4.3) is an extra-tropical cyclone producing heavy rainfall at the edge of the dry core of the Sahara, where rainfall is usually very scarce even if a cyclone passes nearby. Climatological results from all of the identified HPEs are presented in Section 5.

4.1. A severe autumn HPE in the northwestern Sahara

A prominent HPE occurred in the northwestern Sahara on 20–24 November 2014. It is an outstanding event not only because of the vast amounts of rainfall (Fig. 3c), but also because of its aftermath. It first produced massive rainfall and floods near the Atlantic coast, including tens of casualties in Morocco (Saidi et al., 2020; El Khalki et al., 2020) and then penetrated into the Sahara, with an exceptional rainfall amount (Fig. 3d) and floods in this arid region.

This HPE is associated with an exceptionally deep and southward penetrating extratropical surface cyclone that formed over the eastern North Atlantic, offshore Spain (Fig. 3a). The surface cyclone and its propagation are associated with a succession of Rossby wave breaking indicated by PV streamers and cutoffs intruding northwestern Africa. The repetition of PV structures into the same region is associated with a slowdown of the propagation of the cyclone, which then remained rather stationary during most of the HPE duration (Fig. 3a–b). Overall, 58% of the HPE area overlapped with the surface cyclone (Fig. 3a). Only on the last day of the event, the PV streamer and the cyclone moved northeastward into the Mediterranean Sea, and rainfall in the Sahara gradually decreased. Due to the location of the cyclone and because it stalled next to the coastline, a substantial moisture flux from the southeast, associated with an anomaly magnitude of more than two standard deviations in TCW, converged towards the Sahara from both the Atlantic Ocean and Equatorial Africa, surrounding the Atlas Mountains (Fig. 3b), enabling precipitation in this arid region (Rieder, 2023).

During the 5-day rain event a total of $39.6\ \mathrm{km}^3$ of rainfall with an average depth of 47.8 mm, locally consisting of more than 120% of the mean annual precipitation (Fig. 3d), precipitated over an area of $828,000\ \mathrm{km}^2$ in the Sahara. This huge volume of water is similar to 10 months of flow in the Blue Nile (Conway and Hulme, 1993). The HPE duration (Section 3.2) was 82 h, making it one of the longest HPEs we have identified (Section 5.1). Over the most extreme day, an area sized $445,000\ \mathrm{km}^2$, $192,000\ \mathrm{km}^2$, $52,000\ \mathrm{km}^2$ exhibited daily rain intensities locally exceeding the 2-y, 10-y and 100-y return periods, respectively. These values make this event extraordinary in terms of the spatial extent of extreme intensities. Floods associated with this event filled water reservoirs and lakes downstream from the event, filling the typically-empty Sabkhat El-Mellah (see e.g., in MODIS satellites: EOSDIS, 2023; and Mabbutt, 1977, p. 156).

To conclude, extraordinary rainfall was precipitated in the northwestern Sahara during November 2014 in association with a succession of upper-tropospheric PV streamers accompanied by a stationary surface cyclone near the Atlantic coast. This probably enabled moisture transport and convergence into the region, which in combination with the upper-level forcing that induced ascent, triggered heavy precipitation.

4.2. Southern Sahara HPE in July 2010

Another interesting HPE occurred during 18–20 July 2010 in the southeastern part of the Sahara, at the edge of the Sahel. A low-level cyclone formed over the central Sahara (Fig. 4a) and progressed westward, exhibiting a diurnal cycle of deepening in the afternoon–evening and shallowing during the late night–morning (not shown). Similarly, coinciding with the movement of the HPE, elevated moisture levels progressed from east to west (not shown) along the southern flank of an upper-level high (Fig. 4a), such that the eastern side of the southern Sahara was on average much more humid than the western side and also much more humid compared to normal conditions (Fig. 4b). By exhibiting both a westward propagation and a surface low, this HPE seems to have flavours from both monsoonal activity and easterly waves. Similar to the cyclone movement, heavy rainfall also progressed from east to west, first affecting western Sudan and later northern Chad and Niger, with high-intensity precipitation and floods (IRIN-News, 2010). In Chad, this HPE marked the beginning of a very wet period that lasted almost two months, causing many casualties and severely affecting nearly 150,000 people (UNHCR, 2010; Lejeune-Kaba, 2010). Interestingly, over the same days, other HPEs were also occurring north of the above-mentioned HPE, where total column moisture exhibited values greater than four standard deviations above normal conditions (Fig. 4b). These consisted of lower precipitation amounts but a higher proportion compared to the annual mean (Fig. 4d). Here we chose to focus on the largest-area HPE during this period.

The 3-day event brought by a total of $24.0\ \mathrm{km}^3$ of rainfall, with an average depth of 44.2 mm (roughly 40% of the mean annual precipitation; Fig. 4c–d) over an area of $544,000\ \mathrm{km}^2$ in the Sahara (Fig. 4a, d). The HPE duration (Section 3.2) was 57 h. Over the most extreme day, an area sized $115,000\ \mathrm{km}^2$, $34,000\ \mathrm{km}^2$, $6,000\ \mathrm{km}^2$ exhibited daily rain intensities locally exceeding the 2-y, 10-y and 100-y return periods, respectively. Precipitation did not stop when the HPE "ceased", but rather moved to wetter regions. It moved through Mali and Burkina Faso to Guinea and from there to the Atlantic Ocean, causing floods in the non-desert regions along its passage, with more than 30,000 people severely affected (RFI, 2010). In contrast to "normal" HPEs in deserts which arise from the intrusion of a synoptic-scale system from wetter regions (as in the November 2014 case study; Section 4.1), the July 2010 HPE was initiated in the desert and later impacted wetter regions downwind (to the west). The "self-propagation" of monsoonal rainfall with a positive rainfall-surface moistening feedback is a known phenomenon in the West African monsoon region (Taylor et al., 2011) and seems to have manifested in the 2010 monsoon season in the central southern Sahara-Sahel as well.

4.3. Early spring HPE in the dry core of the Sahara

The dry core of the Sahara, where mean annual rainfall is $< 15\ \mathrm{mm\ y}^{-1}$ (Fig. 1), is an area where precipitation is so rare that HPEs are expected to be extraordinary. During 10–13 March 2020, an extensive HPE occurred in the region. An upper-level trough protruded into the northern Sahara, leading to the formation of a surface low (Fig. 5). Initially, the surface low moved southward into the Sahara.

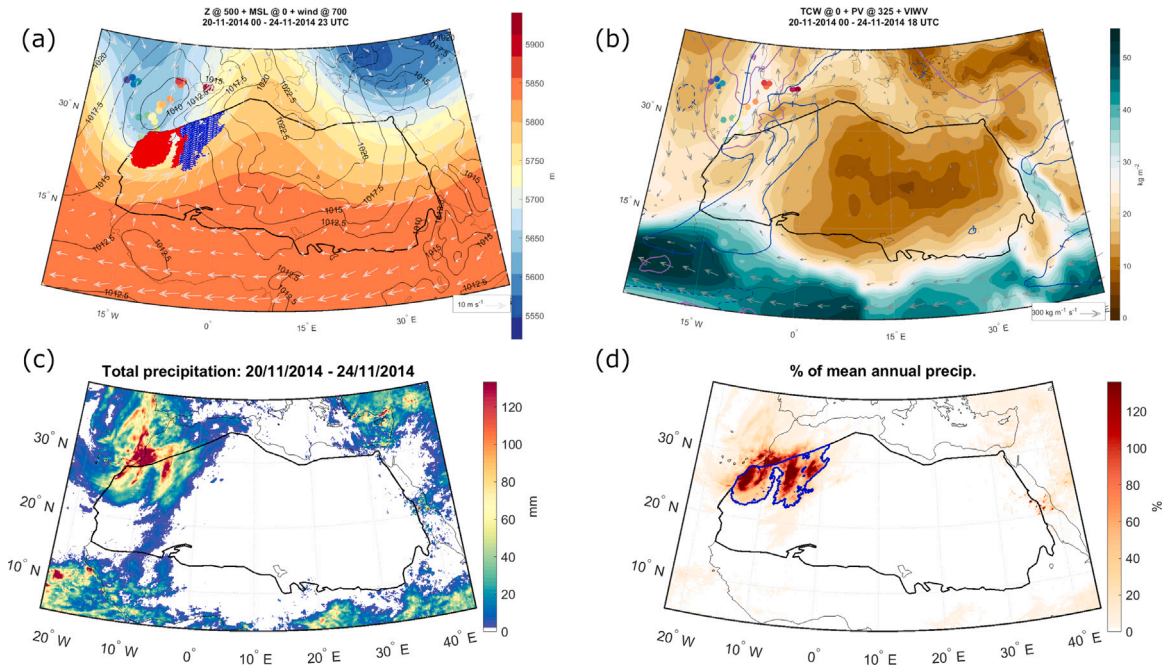

Fig. 3. Synoptic conditions and rainfall during the northwestern Sahara HPE on 20–24 November 2014. (a) Geopotential height at 500 hPa (colours), winds at 700 hPa (arrows), and sea level pressure averaged throughout the duration of the HPE. Also shown are the locations of the centres of the surface cyclone (coloured dots). These display the movement of the cyclone at 6 h intervals (dark blue at 00 UTC on 20 November and dark red at 18 UTC on 24 November). The extent of the 5-day Saharan HPE is dotted in blue and outlined in (d). $\sim 480{,}000$ km^2 (58% of the HPE region) overlaps with a cyclone mask. The overlapping region is highlighted in red. (b) Similar to (a), but with contours of total column water (TCW; colours), the anomaly of TCW compared with the climatology of the specific month is shown in standard deviation units (blue contours), the 2-PVU line at 325 K is in purple. Arrows represent integrated vapour transport (IVT). (c) Rainfall accumulation during the HPE and (d) similar to (c) but as a ratio of the annual mean precipitation. (For interpretation of the references to colour in this figure legend, the reader is referred to the web version of this article.)

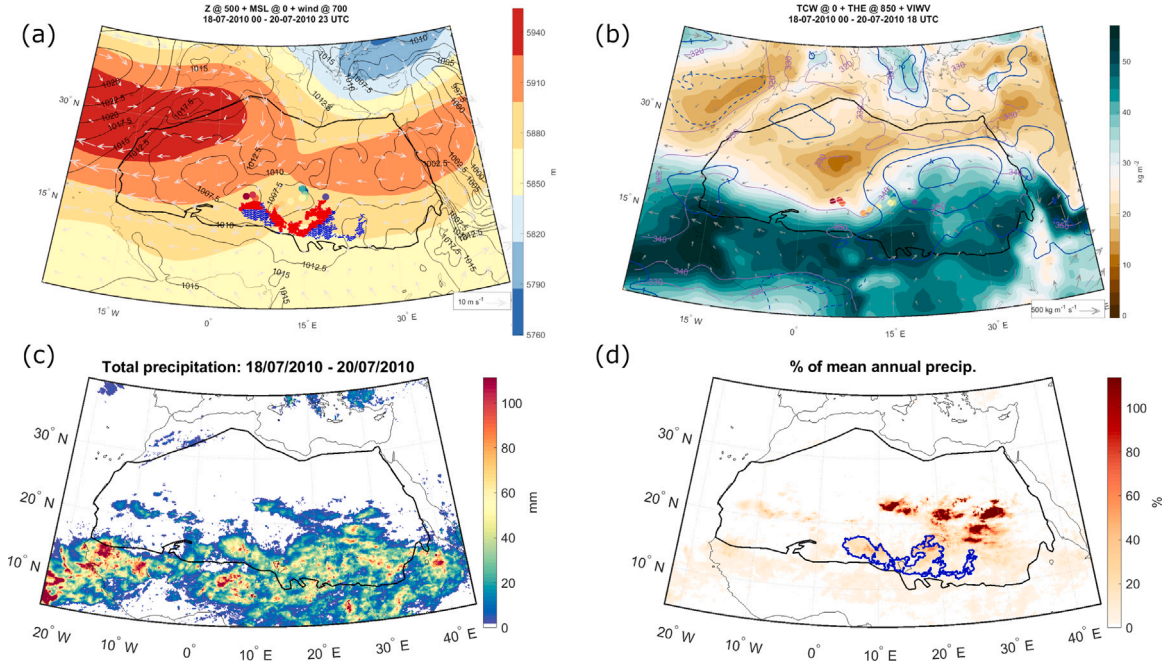

Fig. 4. Similar to Fig. 3, but for the 18–20 July 2010 southern Sahara - Sahel HPE. Also shown is the equivalent potential temperature (b) at 850 hPa (purple contours). 52% out of the $544{,}000$ km^2 of this HPE overlaps with cyclone masks throughout the duration of the event. Note that the same dates were characterised by additional, locally significant, HPEs over the eastern part of the central Sahara (pronounced in d). (For interpretation of the references to colour in this figure legend, the reader is referred to the web version of this article.)

Later, accompanied by an upper-level PV-cutoff that detached from the trough, it swayed north-eastward, toward the Mediterranean Sea, where it deepened and stalled. At its peak, to the north of the Nile Delta, the cyclone reached a minimum pressure of 994 hPa, which ranks it among the deepest Mediterranean cyclones (e.g., Scherrmann et al., 2023). This was also the cyclone stage leading to most of the rainfall during its passage through the northern Sahara, implying that Mediterranean-origin moisture may be involved in this HPE. Moisture was positively anomalous (>2 standard deviations above normal) and moisture flux was substantial (Fig. 5b). At the last stages of the event,

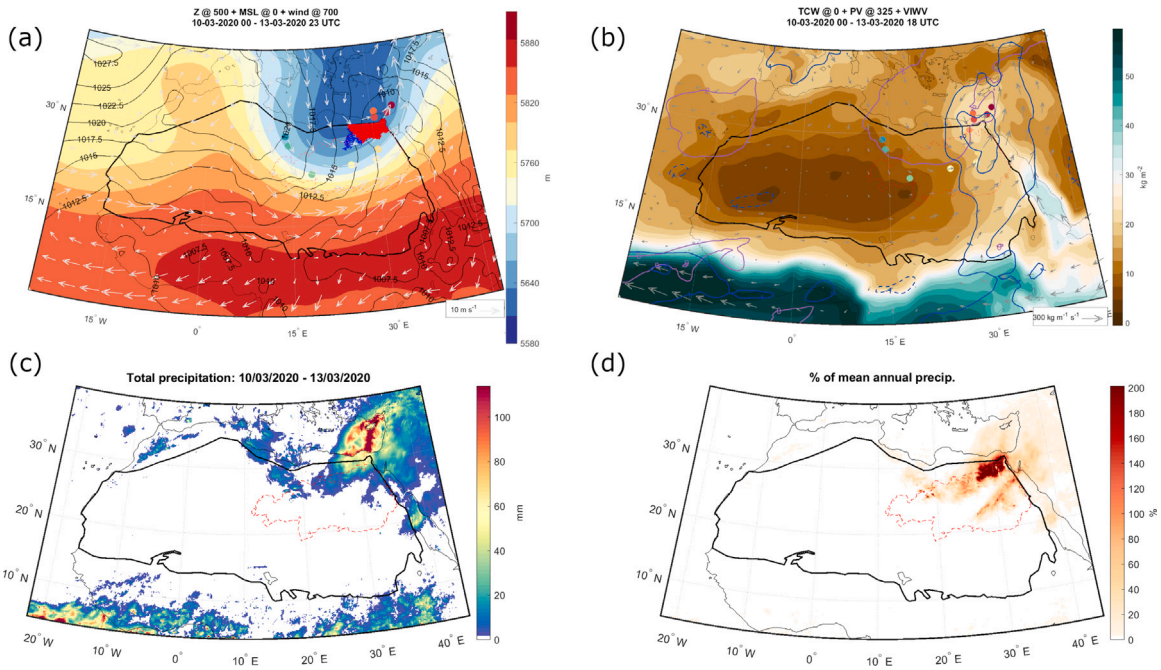

Fig. 5. Similar to Fig. 3, but for the 10–13 March 2020 HPE in the dry core of the Sahara. The 2-PVU line in (b) is at 325 K. 82% out of the 207,000 km^2 of this HPE overlaps with cyclone masks. (For interpretation of the references to colour in this figure legend, the reader is referred to the web version of this article.)

rainfall continued to occur east of the Sahara, yielding the most intense precipitation day for at least 20 years in the Egyptian Sinai Peninsula, as well as flash floods and wind-related damages in Israel (IMS, 2020; Soltani et al., 2022; Mekawy et al., 2023).

Precipitation over the core of the Sahara during this HPE summed to a total volume of 5.1 km^3 (an equivalent to 48% of the annual municipal water demand of Egypt in 2020; FAO, 2023). The mean areal precipitation during this event was 25 mm, well above the yearly average (Fig. 5c, d). The areal extent of this HPE was 207,000 km^2 and it lasted 34.5 h. The extent of the 2-y return period intensity was the same as the event extent, meaning that the event was greater than the 2-y intensity value across its full extent. The extent of the 10-y and 100-y return periods was 151,000 km^2 and 88,000 km^2, respectively. Naturally, estimations for high return periods over such a dry region are less reliable. Nevertheless, these large values point toward a very high extremeness level for this event over the core of the Sahara.

5. Climatology

From these case studies, we learnt that HPEs in the Sahara have the potential to extend over vast areas, to produce massive rainfall amounts even in the dry core of the Sahara, and that surface cyclones can be important for their formation. In this section, we show the results of the climatology of HPEs in the Sahara. We first concentrate on rainfall properties and then on the meteorological conditions during HPEs. The statistics of rainfall properties and the occurrence of HPEs are in Section 5.1, and a statistical analysis of the events' extremeness is in Section 5.2. The distinct synoptic-scale conditions associated with HPEs for the different seasons is presented in Section 5.3, and a specific focus on the link of HPEs to surface cyclones is in Section 5.4.

5.1. HPE properties

During the 21-y study period, HPEs occurred throughout the Sahara (Fig. 6), contributing an average of 29% of the mean annual rainfall, peaking at ~ 70% around the Tropic of Cancer (Fig. A7). Events occurred on 59% of the days during the study period, with a total of 41,978 HPEs identified. Six-hundred-and-fifty of these HPEs occurred over the dry core of the Sahara (Fig. A8), on ~ 5% of days. In this regard, it is important to note that over many of the days, multiple HPEs were identified and that most of them are rather extreme (Section 5.2). The ten largest events throughout the Sahara, and the five largest events in the dry core of the Sahara by precipitation volume are listed in Table 1. A complete list of all other events is archived online: DOI: 10.5281/zenodo.10074760.

The highest density of events is in the southern Sahara–Sahel region, with most events exhibiting on average at least many tens of mm of rainfall (Fig. 6). Conversely, the northern Sahara is characterised by a smaller density of HPEs, as well as lower rainfall accumulations per event. In the northern Sahara, a clear east–west gradient exists; events in the east are generally smaller in spatial extent and lower in rainfall accumulation compared to events in the west, which are generally the largest events by area. In fact, the eight largest identified HPEs occurred in the northwestern Sahara (Fig. 6).

The seasonality of events exhibits regional differences too (Fig. 7). While summer events are much more frequent than events in any other season (69% of identified HPEs), they dominate mainly the southern side of the Sahara. Further north, at about the Tropic of Cancer, events are more evenly distributed among the other seasons, with autumn events (22% of all HPEs) dominating the western side of the desert, winter events (3%) dominating the northeastern side, and spring events (6%) are apparent throughout the northern Sahara, but are most noticeable near the Egyptian–Libyan border at the core of the Sahara. North of the Sahel, several clusters are observed, consisting mainly of summer events (Fig. 7). These clusters appear next to mid-Saharan mountains: the Ahaggar, Aïr and Tibesti Mountains, and between the Ennedi Plateau and the Marrah Mountains (Fig. 1).

Seasonality also affects the diurnal pattern of HPEs. Summer, autumn, and to a lesser degree spring events too, exhibit a pronounced diurnal cycle peaking in the late afternoon–evening (Fig. 8). Peaks are most commonly observed at three times of the day (UTC+1), one at 18:00, another at around 20:00, and a smaller one at 1:00. Furthermore, this diurnal pattern unveils a spatial preference (Fig. A9): throughout most of the southeastern and central Sahara HPEs peak at noon to evening, with several regions showing a progressive peak timing starting at late morning–noon in the east and progressing to

Table 1
Properties of the 10 largest Saharan HPEs, and the 5 largest dry core HPEs.

Rank	Start [yyyymmdd]	End	Date of max. volume	Total area [km^2]	Avg. area [km^2]	Depth [mm]	Volume [km^3]	Duration [h]	Area > 2-y/10-y / 100-y [km^2][a]	Lat [°]	Lon [°]	Cyc. overlap [%][b]	Cyc. dist. [km][c]
1	20031021	20031022	20031021	9.06e+05	7.02e+05	53.1	48.1	41.0	6.39e+05/2.54e+05/6.81e+04	−11.45	23.40	1.1	0
2	20151019	20151024	20151022	6.14e+05	2.01e+05	67.1	41.2	104.0	2.69e+05/1.44e+05/4.52e+04	−8.95	26.00	20.4	0
3	20141120	20141124	20141121	8.28e+05	2.41e+05	47.8	39.6	82.0	4.45e+05/1.92e+05/5.24e+04	−6.21	27.67	51.4	0
4	20200731	20200801	20200801	4.79e+05	3.01e+05	66.2	31.7	31.5	3.27e+05/1.78e+05/5.92e+04	31.00	16.15	0.2	0
5	20090117	20090122	20090121	7.21e+05	1.7e+05	38.9	28	80.0	3.29e+05/2.16e+05/6.07e+04	4.25	28.55	84.4	0
6	20050926	20050929	20050927	6.87e+05	2e+05	43.1	29.6	74.5	1.7e+05/5.64e+04/7.75e+03	−7.95	20.28	52.5	0
7	20100718	20100720	20100719	5.44e+05	1.81e+05	44.2	24	57.5	1.15e+05/3.4e+04/6.12e+03	16.15	14.32	51.9	0
8	20060207	20060212	20060209	5.77e+05	1.29e+05	46.1	26.6	117.0	3.65e+05/1.24e+05/1.55e+04	−8.17	27.20	8.1	0
9	20130809	20130810	20130809	5.21e+05	2.61e+05	36.1	18.8	24.0	1.09e+05/9.65e+03/207	29.25	14.20	1.2	0
10	20190821	20190822	20190822	4.04e+05	2.08e+05	47.2	19.1	47.0	6.31e+04/8.44e+03/457	28.70	12.30	0.0	482
Dry core of the Sahara													
1	20200310	20200313	20200312	2.07e+05	6.2e+04	25	5.17	34.5	2.13e+05/1.51e+05/8.83e+04	30.20	29.20	78.1	0
2	20131210	20131210	20131210	1.74e+05	1.74e+05	13.4	2.34	20.0	1.77e+05/1.18e+05/5.26e+04	14.95	25.45	0.0	1097
3	20200810	20200810	20200810	6.57e+04	6.57e+04	19.5	1.28	11.5	6.52e+04/4.5e+04/6.89e+03	30.25	20.45	7.9	0
4	20200806	20200806	20200806	4.75e+04	4.75e+04	17.5	0.832	11.5	4.73e+04/4.02e+04/1.06e+04	31.35	21.75	0.0	211
5	20161027	20161027	20161027	5.65e+04	5.65e+04	13.3	0.749	12.5	5.87e+04/4.28e+04/3.88e+03	32.75	27.95	0.0	1396

Abbreviations: Avg = average, cyc = cyclone, dist = distance.

[a] The area over which 2, 10 and 100 y return period daily rain intensities were exceeded.

[b] Percentage of the HPE area overlapping with cyclone masks.

[c] Distance between the HPE and the nearest cyclone (0 means overlapping).

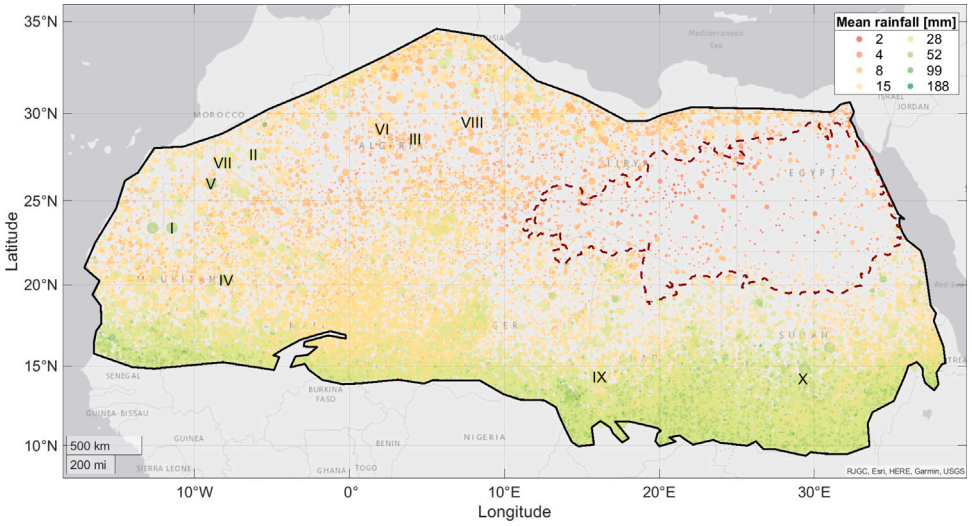

Fig. 6. Identified Saharan HPEs in the 21-y period, marked by their centre of mass of accumulated precipitation. Colours represent mean event rainfall, and the size of the dots represents the area of the HPEs, categorised into 8 and 6 categories in log-scale, respectively. The smallest dots are $\sim 26,000$ events with size $1000 > X > 3900$ km^2 and the largest are 57 events of at least $230,000$ km^2. The 10 largest events by area are labelled with Roman numerals. The second and the tenth largest events are discussed in Section 4.1 and Section 4.2, respectively. A zoom-in over the core of the Sahara (dashed red line) is in Fig. A8. (For interpretation of the references to colour in this figure legend, the reader is referred to the web version of this article.)

the afternoon–late evening, and even night to their west. In contrast, most of the northern and western Sahara reveals a much more erratic pattern, with no clear timing for the daily maximum, aside from some nighttime–morning maxima over part of the region.

This diurnal structure points to a surface-heating-related precipitation mechanism, i.e., deep convection, similar to the pattern seen in the southern Sahara case study (Section 4.2). Compared to wetter regions, the timing of precipitation peaks may seem a bit late during the day, but desert precipitation tends to peak rather late in the evening, since the lower troposphere is relatively dry, hence air needs to ascend to quite high levels to reach saturation and it takes longer for the lower atmosphere to heat until the stability is sufficiently reduced for deep convection to occur (e.g., Otterman and Sharon, 1979; Marra et al., 2022a). In addition, this evening peak (Fig. 8) is slightly lagged after the peak of squall line generation activity, which was found to be highly associated with African easterly waves (Fink and Reiner, 2003).

In contrast, winter events, with much lower average peak intensities, do not exhibit any diurnal pattern (Fig. 8). This suggests that they are controlled mainly by larger-scale weather systems, similar to the northern Sahara case studies (Sections 4.1 and 4.3). The notion of large-scale control on colder months' HPEs is supported by the duration of events as well. While most identified HPEs are shorter than 1 day, regions heavily affected by non-summer HPEs (i.e., the central Sahara and further north, and the western periphery of the Sahara; Fig. 7) coincide with regions with the longest duration HPEs (Fig. A10).

During Saharan HPEs, 31 mm (σ = 14 mm) of rain precipitated over the affected regions, on average, with the largest amounts falling during summer (33 mm on average) and autumn (30 mm) events, and

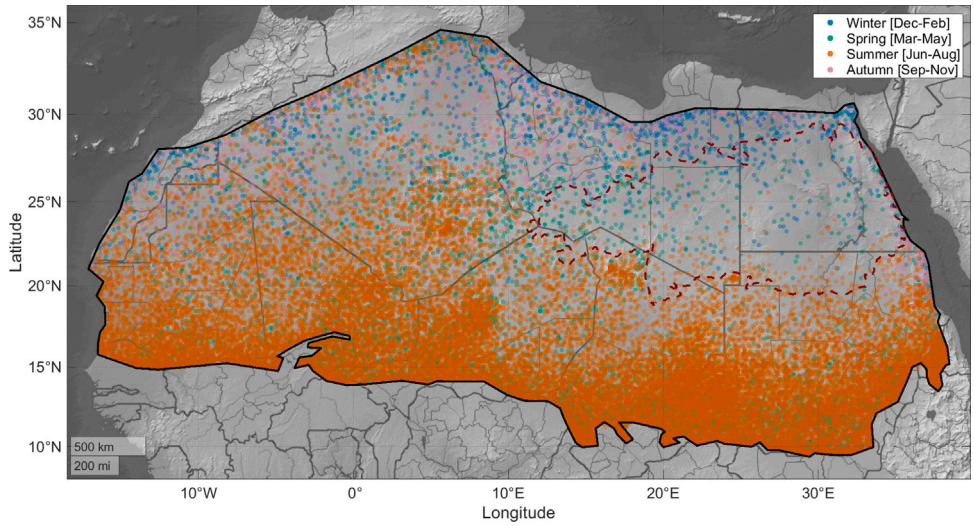

Fig. 7. Seasonal distribution of HPEs. Each dot represents one HPE (as in Fig. 6). Colours represent the season of occurrence. (For interpretation of the references to colour in this figure legend, the reader is referred to the web version of this article.)

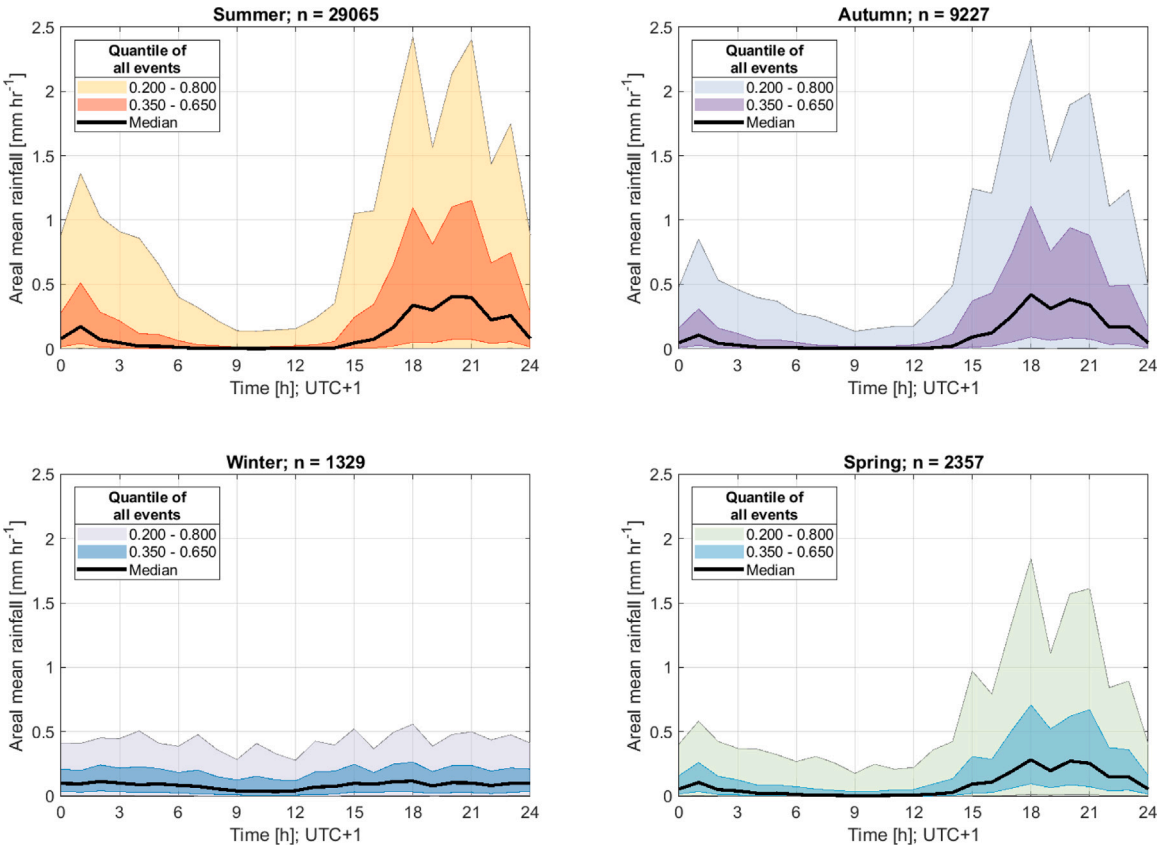

Fig. 8. Diurnal cycle of HPEs. Values are mean areal intensities throughout the HPE regions. The median across events is in bold and the different quantiles are coloured. Each panel represents a different three-month season, and the number of events is given in the panel's title. (For interpretation of the references to colour in this figure legend, the reader is referred to the web version of this article.)

lower amounts characterising winter (15 mm) and spring (23 mm) HPEs (Fig. A11). This pattern corresponds to the spatial distribution of HPEs, where winter and spring events generally occur over the drier portions of the desert. In terms of precipitated volume, however, winter HPEs exhibit the highest values (0.31 km^3, on average), followed by summer (0.30 km^3), autumn (0.24 km^3) and spring (0.20 km^3) (Fig. 9). The greater volume in winter events corresponds (a) to their longer duration: 17 h duration on average for winter events compared to

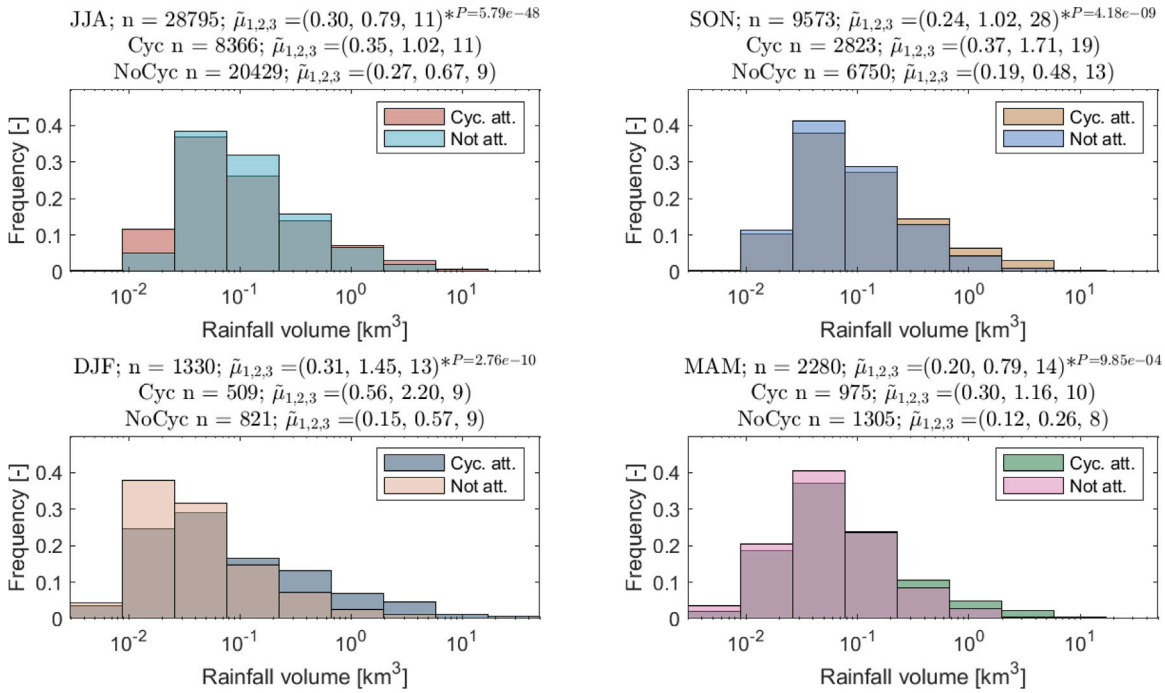

Fig. 9. Rainfall volume during HPEs. Different panels are histograms for the different seasons. For each season, the histogram is divided into HPEs attributed to surface cyclones and HPEs not attributed. Panels' headings are composed of the properties of all HPEs for the season (first row), cyclone-attributed HPEs (second row) and non-attributed HPEs (third row). n is the number of events and $\tilde{\mu}_{1,2,3}$ are the mean, variance, and skewness. Asterisks represent a significant difference between the attributed and non-attributed HPEs (with P-values displayed next to them). (For interpretation of the references to colour in this figure legend, the reader is referred to the web version of this article.)

12–13 h for other seasons' HPEs (Fig. A12), and (b) to their larger areas: 15,000 km^2 on average per winter event, compared to 7600–8200 km^2 (Fig. A13) for the other seasons. The respective meteorological conditions leading to these distinct seasonal patterns are presented in Section 5.3.

5.2. Extremeness of events

Considering the exceptionally high variance of precipitation across the Sahara (e.g., Nicholson, 2011, p. 197), in many regions most events that exceed a few drops of rain can already be considered extreme. Daily rain intensities characterising e.g., the 2-y return periods are often nearly zero (Fig. 10c). Even when considering higher return periods, these values can be relatively low (Fig. 10d, e), especially in the core of the Sahara. However, the "spottiness" of the derived extreme rainfall maps suggests that over the driest regions of the Sahara, even when using the SMEV, which is suitable for use in regions with low rain days frequency, and short observational records, the 21-y IMERG dataset might not be enough to give accurate information over a specific pixel. Nevertheless, when considering larger regions, it seems that the general patterns are probably realistic, with lower intensities over the drier regions for low return periods becoming increasingly higher over high return periods. For example, the intensities for very high return periods over the core of the Sahara, seem to be more intense compared to other, wetter Saharan regions (Fig. A4), in agreement with the heavier distribution tails that characterise such regions (Marra et al., 2017; Morin et al., 2020; Amponsah et al., 2022).

More than 60% of the identified HPEs have daily rainfall intensities that exceed the local 2-y return period, where on average ~ 2600 km^2 were affected by rainfall with this intensity or higher (Fig. 10a). The more extreme return periods, the 10- and 100-y, were exceeded by 24% and 6% of the HPEs, with an average affected area of ~ 550 km^2 and ~ 100 km^2, respectively. This means that while many events were identified (Section 5.1), actually, most of these events are not only "heavy" but can be considered extreme events also in terms of annual exceedance probability. As a comparison, the infamous Western Germany–Belgium floods in July 2021 were a result of an HPE considered to have an especially wide extent: an area of ~ 3300 km^2 exceeded the 100-y return level intensities (Mohr et al., 2023). Here we find 179 events with greater spatial coverage for the 100-y return level intensity. In this regard, the northwestern Sahara case study (Section 4.1) is only the 8th largest event in our dataset, and the case study from the core of the Sahara (Section 4.3) comes in second largest. Given these huge areas affected by severe HPEs, even in a place as sparsely populated as the Sahara, quite a few people might be affected by such events, not to mention potential damages to roads and infrastructure corridors that are the only connection between large but isolated communities in the Sahara (OECD, 2014, pp. 47–50).

Wide-extent extremes occur throughout the Sahara (Fig. 10b). However, the larger spatial extent during winter events (Fig. A13) combined with the more arid location that characterises most of these events (Figs. 1 and 10c–e) make them especially relevant and potentially impactful for the respective regions. The average area exceeding the 10-y return period daily intensity value in winter is 2400 km^2, compared with 400–500 km^2 for summer and autumn events and 1000 km^2 for spring events.

5.3. Meteorological conditions during HPEs

The following is an overview of some climatological characteristics of the atmospheric state during HPEs throughout the Sahara and specifically for its dry core, categorised into four seasons, and with a focus on wintertime events.

Winter. During winter Saharan HPEs, a negative geopotential height anomaly is present in the upper troposphere over the northwestern Sahara (~ −60 m at 500 hPa) and a positive ridge-like anomaly is seen over the eastern Sahara; the upper-level anomaly is accompanied by a negative anomaly of sea level pressure extending from the northwestern Sahara toward the central Sahara (Fig. 11a). This structure is associated with higher-than-normal surface temperatures over the eastern and south-central Sahara and colder surface temperatures over the western Sahara and the Atlas Mountains (Fig. A15). This anomaly structure

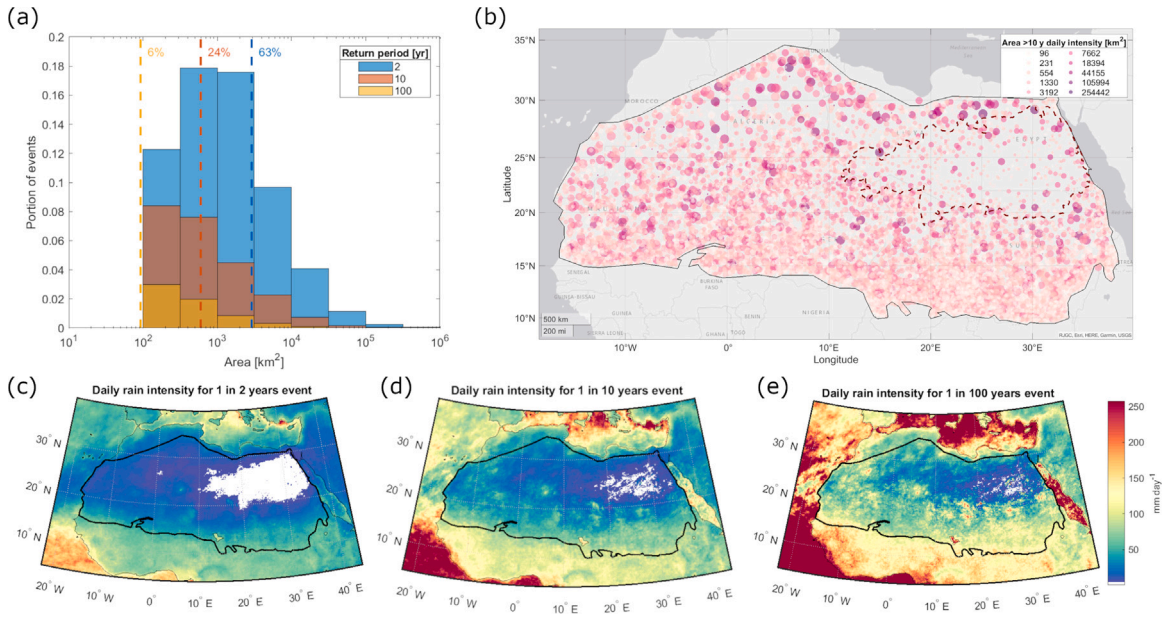

Fig. 10. Extremeness level of identified HPEs. (a) The area above which the return period of the daily intensity of the most intense day during events was at least 2-yr (blue), 10-yr (orange), and 100-yr (yellow). Dashed vertical lines are the average values for each return period, and the numbers next to these lines are the portion of all HPEs that exhibited these extremeness levels. For example, 24% of HPEs exhibited an intensity equal to or greater than the 10-yr return period, with an average of $\sim 600\ \mathrm{km}^2$ experiencing this intensity per event. (b) Spatial distribution of the size of areas experiencing at least 10-yr return period intensities during Saharan HPEs expressed both in colours and in the size of the symbols. Thresholds for the 2-y, 10-y, and 100-y return periods are shown on panels c, d, and e, respectively. (For interpretation of the references to colour in this figure legend, the reader is referred to the web version of this article.)

indicates the important role of extratropical cyclones for winter HPEs and their favourable region of occurrence — the northwestern Sahara; similar to the end-of-autumn case study described in Section 4.1. In front of such upper-level troughs, wind in the upper- and mid-levels backs to a southwesterly flow, bringing elevated moisture content from equatorial latitudes (Fig. A16).

During winter HPEs in the dry core of the Sahara, a similar pattern arises but it is shifted roughly 2000 km to the east. The most negative upper-level geopotential height anomaly is centred over western Egypt and Libya accompanied by a negative sea level pressure anomaly to the east of it, centred over eastern Egypt. This structure is mirrored by a major upper-level ridge-like positive anomaly centred over the western Mediterranean and a pronounced surface positive anomaly over the northwestern Sahara (Fig. 11b). The pronounced upper-level positive anomaly in the western Mediterranean may indicate favourable conditions for cut-off lows over the northeastern Sahara (e.g., Yamazaki and Itoh, 2013). At the same time, anomalous southerly winds in the eastern Sahara in combination with the lifting associated with the cyclone increase atmospheric moisture in the region and enable the formation of clouds and rainfall in this normally-dry region (see also the early spring event detailed in Section 4.3).

Spring to Autumn. Spring, summer, and autumn HPEs are characterised by lower-than-normal surface temperature over the southern Sahara, in combination with elevated moisture content in this region (e.g., Fig. A17). This pattern may be associated with increased cloudiness (and rainfall) in the region, reflecting the high frequency of HPEs in the southern Sahara outside of the cold season. Such HPEs are probably associated with a northward intrusion of the African monsoon, which on HPE days extends a few hundred kilometres north, into the desert (see also Section 4.2). In contrast, during cyclone-associated HPEs in autumn, a dipole pattern in surface temperature oriented east–west is revealed. A roughly −2 °C anomaly over the western Sahara becomes a +2 °C positive anomaly next to the Red Sea (e.g., Fig. A17). A similar pattern with an opposite sign is exhibited in mean sea level pressure anomalies; positive anomaly over the western Sahara and negative anomaly over the eastern Sahara.

Over the core of the Sahara, similarly to winter HPEs, a deep upper-level negative geopotential height anomaly over Libya characterises spring HPEs, which is accompanied by a lower-level negative anomaly over central Egypt (Fig. A14). This pattern is more pronounced during cyclone-associated HPEs compared to all HPEs. In accordance with the upper-level trough structure, moisture is elevated from the southwest of the region towards its northeastern side (not shown). Autumn HPEs in the dry core of the Sahara show similar anomaly structures but with a much lower amplitude. Summer HPEs in the region are slightly different, exhibiting a negative upper-level anomaly over northern Libya–Tunisia which is situated to the west of a surface negative anomaly. Over the core of the Sahara, however, a positive sea level pressure anomaly is observed, centred over the eastern Mediterranean. In combination with increased surface temperature (~3 °C) over the region and a decrease in the northerly winds at low levels (~3 m s^{-1}, on average) this suggests a weak Persian Trough formation and reduction of the Etesian–Harmattan winds.

5.4. Relationship of HPEs with cyclones

A large portion of the identified HPEs can be associated with surface cyclones (30%; Fig. 12), with 13% of the HPEs directly overlapping a cyclone mask. Given the high frequency of cyclones in summer, associated with the semi-permanent Saharan heat low and the African monsoon, it is expected that a large portion of summer HPEs will be associated with cyclones. Indeed, in summer and autumn, 29% of HPEs are associated with cyclones. It is, however, in winter and spring that more HPEs are associated with cyclones, with association values of 38% and 43%, respectively.

The fraction of HPEs associated with cyclones is high throughout the Sahara (Fig. 12a). This fraction remains high even when subtracting the average frequency of cyclones (Fig. 12b), especially over the northwestern Sahara, the Ahaggar Mountains, north of the Tibesti Mountains, and along the Egyptian part of the Nile. In contrast, the southeastern and to a lesser degree also the southwestern Sahara show a much lower association of HPEs and cyclones. The southeastern Sahara is actually exhibiting negative anomalies, but these may be related to the

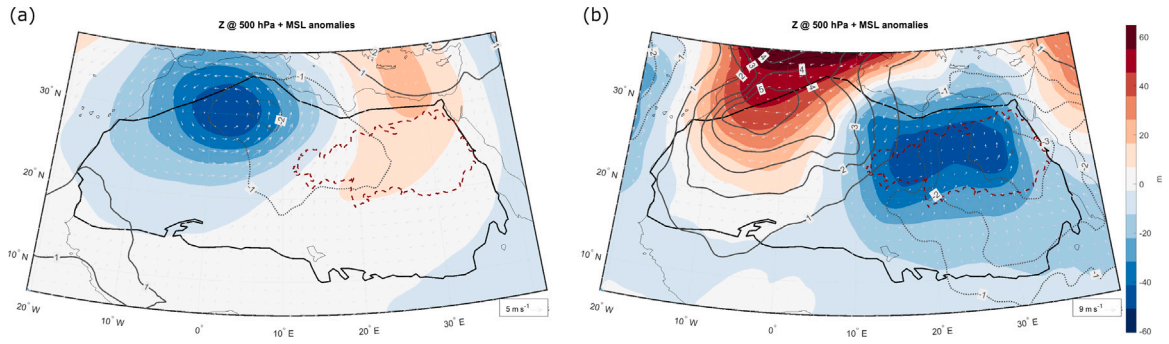

Fig. 11. Composite anomaly during winter events (a) throughout the Sahara, and (b) in the dry core of the Sahara. Coloured contours are geopotential height anomalies at 500 hPa in winter (DJF). Similarly, grey contours are sea level pressure anomalies (dashed when negative; zero line omitted) and arrows are 700 hPa wind anomalies. Composites represent the 10% HPEs with the highest precipitation volume. Anomalies for the other seasons are shown in Fig. A14. (For interpretation of the references to colour in this figure legend, the reader is referred to the web version of this article.)

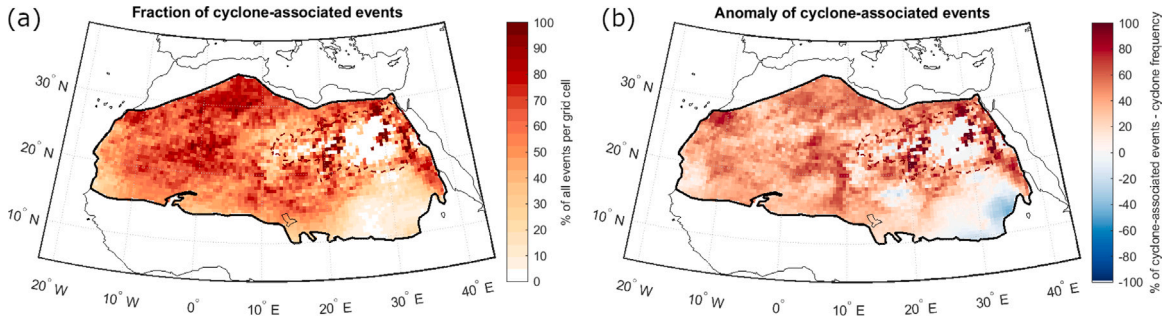

Fig. 12. HPE association with cyclones. (a) fraction of HPEs associated with a cyclone, and (b) the anomaly of this fraction compared to the frequency of cyclones. Similar maps for the different seasons are in Fig. A18 and A19. (For interpretation of the references to colour in this figure legend, the reader is referred to the web version of this article.)

tendency of the cyclone identification algorithm to produce lows over high-elevation regions — in this case, the Ethiopian Highlands. Winter and spring cyclone-associated HPEs occur mainly along the northern side of the Sahara, while the southern Sahara exhibits at places negative association anomalies (Fig. A18 and A19). In contrast, the summer cyclone-HPE association anomaly is large further south, with the largest values found in the northernmost region where HPEs occur, slightly north of the Tropic of Cancer. North of that, the few HPEs occurring exhibit a negative association with cyclones (Fig. A19a). Autumn HPEs show the highest anomalies a bit further south, at around 20° N and in the northwestern Sahara (Fig. A19b).

Rainfall patterns during cyclone-associated HPEs differ from those of the other HPEs (Fig. 9, Fig. A13). The mean volume of cyclone-associated HPEs is higher by 49% (0.36 km^3 compared with 0.24 km^3 for the non-associated events), and the mean spatial extent is larger by 69% ($11.1 \cdot 10^3$ km^2 compared with $6.6 \cdot 10^3$ km^2). The duration for both types of HPEs is rather similar — 12 h for the cyclone-associated events compared with 13 h for the non-associated events, while the area exceeding the 10-yr return period is much higher in cyclone-associated events (1000 km^2 compared with 300 km^2 for the non-associated events; not shown).

6. Discussion

6.1. Heavy precipitation events where there is almost no rainfall

The Sahara is often thought of as a place where surface rainfall hardly ever occurs. On average – from a local-scale perspective – this is close to being true. However, given the vast extent of the Sahara, when adopting an event-based perspective, we showed that HPEs occur in more than half of the days somewhere across the desert (Fig. 6). Even when considering the dry core of the Sahara, where there is nearly zero rainfall, events occur on ∼ 5% of the days. Such events can have significant effects on the local population, infrastructure, and the surface hydrology and geomorphology of the impacted region. The November 2014 event in the northwestern Sahara (Section 4.1) is a good example of such impacts. Its resultant floods severely impacted the local population, leaving behind much damage, but also filling surface water reservoirs and lakes. Relevant questions in this regard are whether such events are predictable and can be warned from? Can we make better use of the available surface water before it evaporates? What is the contribution of such events to underground aquifers? While these questions are not the scope of this work, here we provide both a way to identify desert HPEs and a comprehensive list of HPEs, which can be used to answer such questions in future studies.

Generalised characteristics of Saharan HPEs are given in Fig. 13, in which the Sahara is arbitrarily divided into four regions. The frequency of events decreases clockwise from the southeastern part of the Sahara to the northeastern dry core of the desert. Likewise, the mean rainfall in events decreases in the same manner (lower right quadrants in Fig. 13), and the dominant season of HPEs changes from summer in the southeast to autumn in the west, winter in the north, and spring in parts of the northeast. The area of events exhibits a west-east gradient, with larger events in the western Sahara. Lastly, the importance of cyclones is clear in all regions except the southeastern one, and it is highest in the northwest.

The dominance of cyclones during HPEs is relevant for the predictability of such HPEs. Given the synoptic-scale evolution of cyclones, these precursors usually appear 1–5 days in advance (e.g., Keil et al., 2020). In regions where cyclones are dominant drivers of heavy rainfall, events are likely to have higher predictability compared to other regions and to events not related to the presence of a surface cyclone. In contrast, in summer, and where the prevalence of cyclones is only weakly associated with HPEs, the predictability of HPEs is likely lower. There, rainfall is mainly associated with diurnal convection, which may require the use of a convection-permitting model, but it also requires

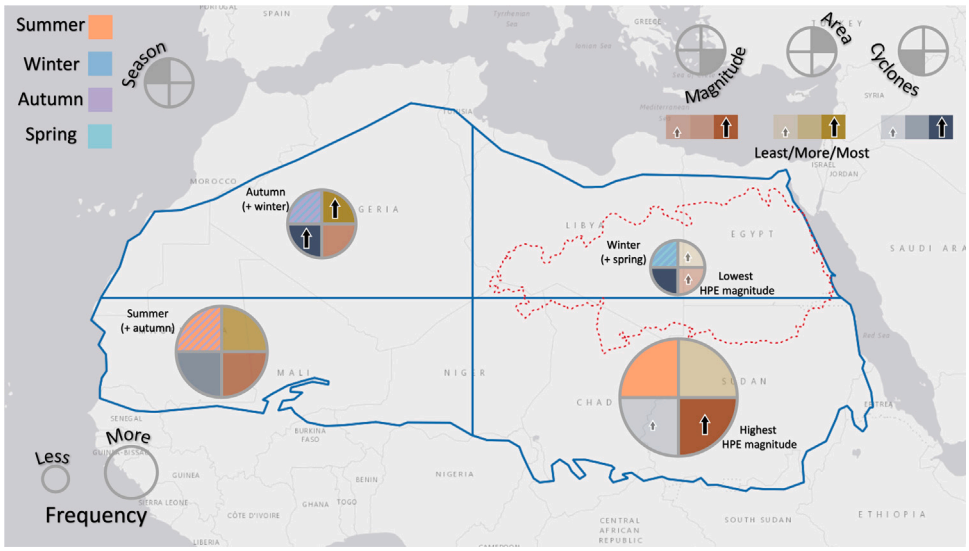

Fig. 13. General schematic representation of major rainfall properties in different regions across the Sahara. Shown are the frequency of HPEs, represented by the size of the circles, the main rainfall season (colours; upper-left quadrant), the relative area of HPEs (colour strength; upper-right quadrant), the magnitude of events (colour strength; lower-right quadrant), and the fraction of surface cyclones associated with HPEs (colour strength; lower-left quadrant). Large and small arrows represent the regions where the respective properties are highest and lowest. Please note that colours vary also in between these two extremes. (For interpretation of the references to colour in this figure legend, the reader is referred to the web version of this article.)

much information about the initial and boundary conditions, which makes it even harder to predict (e.g., Rinat et al., 2021). Given the database of HPEs we provide here, this could be relatively readily obtained, using, e.g., ECMWF's extreme forecast index (EFI; Lalaurette, 2003) and examining the lead time of cyclone-associated vs. non-associated HPEs with high EFI in the different regions and seasons as presented here (e.g., Fig. 13).

HPEs tend to cluster in time and space (e.g., Fig. 7). While this can be a result of the identification scheme used here – in case the buffer region is too small and since we search for overlap of close-by events – we suggest that this is mainly because some atmospheric processes are more prone to generating HPEs than others. Many studies have examined warm-season HPEs, mainly in the southern Sahara and its vicinity, in connection with the African Monsoon, African easterly waves, and the Saharan heat low (see Section 1.1). However, the factors involved in heavy precipitation in other seasons and in other regions of the desert remain somewhat obscure. Here, we recognised these events and showed their association with surface cyclones. When surface cyclones are present, HPEs produce larger rain volumes and their spatial extent is larger, especially in winter (Fig. 9). Some of the largest HPEs in the Sahara (in terms of both volume and extent) are a result of surface cyclones stalling in the vicinity of the Sahara (e.g., Sections 4.1 and 4.3). Periods with a repeated arrival of upper-tropospheric PV structures (streamers or cutoffs) to the same area tend to generate such slow-moving/stationary cyclones, and therefore more intense HPEs. In contrast, periods in which surface cyclones are not present tend to produce fewer HPEs, and the HPEs that do occur are smaller in size and magnitude. Importantly, this means that a better understanding of synoptic-scale features in the vicinity of the Sahara can help in comprehending, and hopefully also predicting, the occurrence and behaviour of HPEs in the desert.

Similar atmospheric processes control HPEs inside and adjacent to the Sahara. Monsoon rains are probably related to most of the HPEs we see in the Sahara, mainly in its southernmost part. Intriguingly, monsoon-related HPEs in the Sahara exhibit a remarkable behaviour whereby they cannot only permeate the desert but also move out of it, exerting substantial influence on adjacent wetter areas (Section 4.2). Analogously, extratropical disturbances intruding into the Sahara may move out of it and produce heavy rainfall in nearby regions (Section 4.3). The genesis of cyclones in the Sahara and their impacts outside the Sahara is well known for Sharav (Alpert and Ziv, 1989) and Mediterranean cyclones (Campins et al., 2011), dust outbreaks (Gkikas et al., 2015), and for Soudano-Saharan depressions (Schepanski and Knippertz, 2011), but these are generally not associated with severe HPEs outside the Sahara.

The limited mechanistic knowledge about precipitation in deserts in general, and in the Sahara in particular, hinders climate change adaptation strategies. The largest relative increase in mean precipitation outside the polar regions is reported for the Sahara and its vicinity. By the end of the 21st century, the projected change in the Sahara has a median value of +39.9% with an SSP5-8.5 pathway, compared to 1850–1900, with confidence intervals in the range of –18% to +214%, as well as a −8.2 d (−52.2 d to +10.0 d) change in consecutive dry days (IPCC, 2021). These uncertainty ranges are huge. Practically, it stresses the inability of climate models to represent small-scale convective processes (e.g., Almazroui et al., 2018), and, therefore, reliable projections of desert precipitation are absent. A first step toward closing this gap is recognising Saharan HPEs and understanding their triggering mechanisms. With the now available list of Saharan HPEs, this may be easier to do. Moreover, the association of surface cyclones in such events is revealed by our analyses. Still, we stress that other synoptic (and smaller scale) systems are also relevant for many of the Saharan HPEs, and are yet to be thoroughly explored.

The potential effects of individual HPEs are specifically important in drylands. Recently, in a global analysis of extreme rain seasons, Flaounas et al. (2021) showed that while extreme seasons in the arid parts of the globe exhibit much more precipitation than typical years (far more than in other climates), these seasons result from the addition of only a few rain days. Such rain days are exactly the HPEs we explored here, which further emphasise the importance of analysing their relationship with synoptic-scale systems.

6.2. Reliability of IMERG results

Saharan HPEs are generally short-lived and local, and are therefore hard to capture using rain gauges. Such "spotty" events may be missed even by satellite precipitation estimations, suggesting that our analysis might be underestimating the number of events. A recent analysis of events throughout the continental USA showed that only ~ 50% of events are identified by IMERG (Li et al., 2023). However, events in

this analysis are defined based on 30-min data and are identified as pixel-based events. Thus, possible spatial mismatches and longer-term temporal mismatches are accounted as false identifications. A similar analysis in Brazil showed that IMERG events have too-long duration and too-low intensity (Freitas et al., 2020). In our case, events are based on daily rainfall and are identified using a clustering of rainy pixels in space and time — possibly decreasing the number of "undetected" events, compared with a pixel-based, 30-min resolution, identification scheme.

Nevertheless, many issues can prevent us from correctly identifying events and accurately determining their rainfall properties. Accurate rain rates in IMERG depend on low-Earth-orbit satellite revisits, which are limited to once every few hours. This means that rain intensity biases are expected, as well as under-detection of very short events. However, with respect to alternative approaches – sparse rain gauges, model reanalysis, and post-event indirect estimates – satellite QPEs remain the most viable. Our intention here is not to validate satellite-derived rainfall estimations, but rather to identify HPEs and understand their properties and association with cyclones. Therefore, even if some events are missing, and rain intensities are not extremely accurate, we do not expect to have a significant one-sided bias, meaning that our climatology probably represents well Saharan HPEs. Two exceptions for this could be (a) the very small-scale events: short events (up to ~ 3 h), might be missing due to the limited temporal resolution of satellite observations, and the small spatial scale events (<1000 km^2) might be missing because of the spatial threshold we set, and (b) below-cloud evaporation may yield a positive bias of satellite-based QPEs, although this is expected to be lower when using products partially based on active radar measurements, where precipitation is observed all the way to the ground (e.g., Amitai et al., 2012).

Given the high variability of rainfall in arid regions, the extremeness of events is harder to assess compared to wetter regions. Results of extreme value analyses depend more heavily on the choice of the extreme value model (Tabari, 2021). Furthermore, when addressing the driest regions, as we did in the core of the Sahara, our perspective on what determines extreme events needs to be adapted. In regions where rain events happen e.g., once a year or even less (as in Minya, Egypt; Fig. A4), the 2-y event, which for example in Zurich – where the mean number of rainy days is 130 – is the event that happens on average once every 260 events (or the 99.7th quantile) becomes an event that happens on average every other rainy day. Can we still consider this as an extreme event? What about the event that happens once in 10 years? This event happens on average once every 10 events — is this an extreme? In terms of its potential effect, we would like to claim that it is certainly an extreme event since its magnitude easily triggers flash floods in such an arid environment (e.g., Zoccatelli et al., 2019). A further complication arises when comparing extreme values from gauge measurements with satellite-derived estimations. On the one hand, since point-scale measurements are not a spatial average, they are bound to be more extreme compared to pixel-based estimates. On the other hand, pixel-based values have a larger chance of capturing the occurrence of precipitation extremes, which may be missed at the point scale by rain gauges. Lastly, while 21 years of data may be enough to represent precipitation climatology and extremes (Marra et al., 2020), it may not be enough in regions where so few rain days exist, as in the core of the Sahara. Therefore, the effects of individual events on the assessment of extreme precipitation in the core of the Sahara are large, and reduced uncertainty is expected only with additional observation years. For that matter, the continuity of presently available satellite-based precipitation estimations (Kidd et al., 2021) is critical.

7. Conclusions

There is little rainfall in the Sahara, much of it falling in discrete, sometimes torrential rain events. In this study, we combined remote-sensing, climatology, statistics, and synoptic meteorology analyses and identified more than 40 k HPEs over the past 21 years, with a few hundred of them occurring over the dry core of the Sahara. In this part of the world, almost every rain can be considered an extreme event. The key conclusions from our study are:

- HPEs occur throughout the Sahara, on average, every other day.
  - The highest density of events is in the southern Sahara - Sahel region. These are predominantly convective events occurring during summer, which are related to the African monsoon and to the Saharan heat low.
  - Colder seasons' events are focused to the north of the Tropic of Cancer. Their duration is longer and they are often associated with surface cyclones.
  - Cyclones penetrating the dry core of the Sahara are associated with HPEs even within this hyperarid expanse.
- HPEs throughout most of the Sahara are anomalously associated with surface cyclones, mostly in the northern side of the desert. Cyclone-associate HPEs are characterised by higher rainfall volume and larger spatial extent, especially in winter.
- Most of the identified HPEs exhibit daily intensities larger than the 2-y return period, with 6% of events exhibiting $\geq$ 100-y intensities.

Since desert HPEs are typically short-lived, localised, and are a consequence of small-scale processes, a better association of HPEs with synoptic systems can help in understanding climate change effects on rainfall in the desert. Moreover, events associated with synoptic scale systems may have increased predictability. For that purpose, the compiled list of identified HPEs, which is available for download, can serve as a valuable resource for future studies.

CRediT authorship contribution statement

Moshe Armon: Conceptualization, Methodology, Data curation, Formal analysis, Funding acquisition, Writing – original draft. **Andries Jan de Vries:** Conceptualization, Writing – Review and Editing. **Francesco Marra:** Conceptualization, Methodology, Data curation, Formal analysis, Writing – Review and Editing. **Nadav Peleg:** Methodology, Data curation, Formal analysis, Writing – Review and Editing. **Heini Wernli:** Conceptualization, Funding acquisition, Writing – Review and Editing.

Declaration of competing interest

The authors declare the following financial interests/personal relationships which may be considered as potential competing interests: Moshe Armon reports financial support was provided by the ETH Zurich Foundation, partially funded by the Stiftung für naturwissenschaftliche und technische Forschung.

Data availability

The list of identified HPEs and their properties is available online at DOI: https://doi.org/10.5281/zenodo.10074760.

Acknowledgements

MA was supported by an ETH Zürich Postdoctoral Fellowship (Project No. 21-1 FEL-67), by the Stiftung für naturwissenschaftliche und technische Forschung and the ETH Zürich Foundation. We would like to thank Dr. Lukas Papritz for help with formalising the Monte Carlo simulations, Dr. Michael Sprenger for helpful tips, discussions and his help with the data used in this study, Yuval Shmilovitz and Prof. Efrat Morin for fruitful discussions, and Dr. George J. Huffman and Dr. Zhong Liu for their help with IMERG data. We would also like to that two anonymous reviewers for their helpful comments.

Appendix A. Supplementary data

Supplementary material related to this article can be found online at https://doi.org/10.1016/j.wace.2023.100638.

References

Al-Falahi, A.H., Saddique, N., Spank, U., Gebrechorkos, S.H., Bernhofer, C., 2020. Evaluation the performance of several gridded precipitation products over the highland region of yemen for water resources management. Remote Sens. 12 (18), http://dx.doi.org/10.3390/RS12182984.

Almazroui, M., Raju, P.V., Yusef, A., Hussein, M.A., Omar, M., 2018. Simulation of extreme rainfall event of November 2009 over Jeddah, Saudi Arabia: The explicit role of topography and surface heating. Theor. Appl. Climatol. 132 (1–2), 89–101. http://dx.doi.org/10.1007/s00704-017-2080-2.

Alpert, P., Shay-EL, Y., 1994. The moisture Source for the Winter Cyclones in the Eastern Mediterranean. Israel Meteorol. Res. Pap. 5, 20–27.

Alpert, P., Ziv, B., 1989. The Sharav Cyclone: Observations and some theoretical considerations. J. Geophys. Res. 94 (D15), 18495–18514. http://dx.doi.org/10.1029/jd094id15p18495.

Amitai, E., Unkrich, C.L., Goodrich, D.C., Habib, E., Thill, B., 2012. Assessing satellite-based rainfall estimates in semiarid watersheds using the USDA-ARS Walnut Gulch gauge network and TRMM PR. J. Hydrometeorol. 13 (5), 1579–1588. http://dx.doi.org/10.1175/JHM-D-12-016.1.

Ammar, K., El-Metwally, M., Almazroui, M., Abdel Wahab, M.M., 2014. A climatological analysis of Saharan cyclones. Clim. Dynam. 43 (1–2), 483–501. http://dx.doi.org/10.1007/s00382-013-2025-0.

Amponsah, W., Dallan, E., Nikolopoulos, E.I., Marra, F., 2022. Climatic and altitudinal controls on rainfall extremes and their temporal changes in data-sparse tropical regions. J. Hydrol. 612 (PA), 128090. http://dx.doi.org/10.1016/j.jhydrol.2022.128090.

Armon, M., Dente, E., Smith, J.A., Enzel, Y., Morin, E., 2018. Synoptic-scale control over modern rainfall and flood patterns in the Levant drylands with implications for past climates. J. Hydrometeorol. 19 (6), 1077–1096. http://dx.doi.org/10.1175/JHM-D-18-0013.1.

Armon, M., Marra, F., Enzel, Y., Rostkier-Edelstein, D., Morin, E., 2020. Radar-based characterisation of heavy precipitation in the eastern Mediterranean and its representation in a convection-permitting model. Hydrol. Earth Syst. Sci. 24, 1227–1249. http://dx.doi.org/10.5194/hess-24-1227-2020.

Ashbel, D., 1938. Great floods in Sinai Peninsula, Palestine, Syria and the Syrian Desert, and the influence of the Red Sea on their formation. Q. J. R. Meteorol. Soc. 64 (277), 635–639.

Awad, A.M., Almazroui, M., 2016. Climatology of the winter Red Sea Trough. Atmos. Res. 182, 20–29. http://dx.doi.org/10.1016/j.atmosres.2016.07.019.

Bagnold, R.A., 1990. Sand, Wind, and War. The University of Arizona Press, Tucson, p. 209. http://dx.doi.org/10.2307/j.ctv2fcct9k.

Barth, H.-J., Steinkohl, F., 2004. Origin of winter precipitation in the central coastal lowlands of Saudi Arabia. J. Arid Environ. 57 (1), 101–115. http://dx.doi.org/10.1016/S0140-1963(03)00091-0.

Beck, H.E., Vergopolan, N., Pan, M., Levizzani, V., Van Dijk, A.I., Weedon, G.P., Brocca, L., Pappenberger, F., Huffman, G.J., Wood, E.F., 2017. Global-scale evaluation of 22 precipitation datasets using gauge observations and hydrological modeling. Hydrol. Earth Syst. Sci. 21 (12), 6201–6217. http://dx.doi.org/10.5194/hess-21-6201-2017.

Campins, J., Genovés, A., Picornell, M.a., Jansà, A., 2011. Climatology of Mediterranean cyclones using the ERA-40 dataset. Int. J. Climatol. 31, 1596–1614. http://dx.doi.org/10.1002/joc.2183.

Chaqdid, A., Tuel, A., Fatimy, A.E., Moçayd, N.E., 2023. Extreme rainfall events in Morocco: Spatial dependence and climate drivers. Weather Clim. Extremes 40 (November 2022), 100556. http://dx.doi.org/10.1016/j.wace.2023.100556.

Chauvin, F., Roehrig, R., Lafore, J.P., 2010. Intraseasonal variability of the Saharan heat low and its link with midlatitudes. J. Clim. 23 (10), 2544–2561. http://dx.doi.org/10.1175/2010JCLI3093.1.

Clarke, F.E., 1973. The great Tunisian flood. J. Res. U.S. Geol. Surv. 1 (1), 121–124, URL http://pubs.er.usgs.gov/publication/70159880.

Conway, D., Hulme, M., 1993. Recent fluctuations in precipitation and runoff over the Nile sub-basins and their impact on main Nile discharge. Clim. Change 25 (2), 127–151. http://dx.doi.org/10.1007/BF01661202.

Copernicus, 2023. Storm Daniel causes flooding in Libya. URL https://www.copernicus.eu/en/media/image-day-gallery/storm-daniel-causes-flooding-libya.

Dayan, U., Nissen, K., Ulbrich, U., 2015. Review article: Atmospheric conditions inducing extreme precipitation over the eastern and western Mediterranean. Nat. Hazards Earth Syst. Sci. 15 (11), 2525–2544. http://dx.doi.org/10.5194/nhess-15-2525-2015.

Dayan, U., Ricaud, P., Zbinden, R., Dulac, F., 2017. Atmospheric pollution over the eastern Mediterranean during summer - A review. Atmos. Chem. Phys. 17 (21), 13233–13263. http://dx.doi.org/10.5194/acp-17-13233-2017.

de Vries, A.J., 2021. A global climatological perspective on the importance of Rossby wave breaking and intense moisture transport for extreme precipitation events. Weather Clim. Dyn. 2 (1), 129–161. http://dx.doi.org/10.5194/wcd-2-129-2021.

Dezfuli, A.K., Ichoku, C.M., Huffman, G.J., Mohr, K.I., Selker, J.S., van de Giesen, N., Hochreutener, R., Annor, F.O., 2017. Validation of IMERG precipitation in Africa. J. Hydrometeorol. 18 (10), 2817–2825. http://dx.doi.org/10.1175/JHM-D-17-0139.1.

Dinku, T., Ceccato, P., Connor, S.J., 2011. Challenges of satellite rainfall estimation over mountainous and arid parts of east Africa. Int. J. Remote Sens. 32 (21), 5965–5979. http://dx.doi.org/10.1080/01431161.2010.499381.

D'Odorico, P., Bhattachan, A., 2012. Hydrologic variability in dryland regions: Impacts on ecosystem dynamics and food security. Philos. Trans. R. Soc. London. Ser. B, Biol. Sci. 367 (1606), 3145–3157. http://dx.doi.org/10.1098/rstb.2012.0016.

El-Fandy, M.G., 1946. Barometric lows of cyprus. Q. J. R. Meteorol. Soc. 72 (314), 291–306. http://dx.doi.org/10.1002/qj.49707231406.

El Khalki, E.M., Tramblay, Y., Massari, C., Brocca, L., Simonneaux, V., Gascoin, S., Saidi, M.E.M., 2020. Challenges in flood modeling over data-scarce regions: How to exploit globally available soil moisture products to estimate antecedent soil wetness conditions in Morocco. Nat. Hazards Earth Syst. Sci. 20 (10), 2591–2607. http://dx.doi.org/10.5194/nhess-20-2591-2020.

Engelstaedter, S., Washington, R., Flamant, C., Parker, D.J., Allen, C.J., Todd, M.C., 2015. The Saharan heat low and moisture transport pathways in the central Sahara—Multiaircraft observations and Africa-LAM evaluation. J. Geophys. Res. 120 (10), 4417–4442. http://dx.doi.org/10.1002/2015JD023123.

EOSDIS, 2023. NASA worldview. URL https://go.nasa.gov/3o1ShGe.

FAO, 2023. AQUASTAT - FAO's Global Information System on Water and Agriculture: Country statistics. URL https://tableau.apps.fao.org/views/ReviewDashboard-v1/country_dashboard?%3Aembed=y&%3AisGuestRedirectFromVizportal=y.

Fink, A.H., Knippertz, P., 2003. An extreme precipitation event in southern Morocco in spring 2002 and some hydrological implications. Weather 58 (10), 377–387. http://dx.doi.org/10.1256/wea.256.02.

Fink, A.H., Reiner, A., 2003. Spatiotemporal variability of the relation between African Easterly Waves and West African Squall Lines in 1998 and 1999. J. Geophys. Res.: Atmos. 108 (11), 1–17. http://dx.doi.org/10.1029/2002jd002816.

Flaounas, E., Röthlisberger, M., Boettcher, M., Sprenger, M., Wernli, H., 2021. Extreme wet seasons – Their definition and relationship with synoptic-scale weather systems. Weather Clim. Dyn. 2 (1), 71–88. http://dx.doi.org/10.5194/wcd-2-71-2021.

Freitas, E.d.S., Coelho, V.H.R., Xuan, Y., Melo, D.d.C., Gadelha, A.N., Santos, E.A., Galvão, C.d.O., Ramos Filho, G.M., Barbosa, L.R., Huffman, G.J., Petersen, W.A., Almeida, C.d.N., 2020. The performance of the IMERG satellite-based product in identifying sub-daily rainfall events and their properties. J. Hydrol. 589 (June), 125128. http://dx.doi.org/10.1016/j.jhydrol.2020.125128.

Fröhlich, L., Knippertz, P., Fink, A.H., Hohberger, E., 2013. An objective climatology of tropical plumes. J. Clim. 26 (14), 5044–5060. http://dx.doi.org/10.1175/JCLI-D-12-00351.1.

Funk, C., Hoell, A., Shukla, S., Husak, G., Michaelsen, J., 2016. The East African monsoon system: Seasonal climatologies and recent variations. Springer Climate 163–185. http://dx.doi.org/10.1007/978-3-319-21650-8_8.

Gkikas, A., Houssos, E.E., Lolis, C.J., Bartzokas, A., Mihalopoulos, N., Hatzianastassiou, N., 2015. Atmospheric circulation evolution related to desert-dust episodes over the Mediterranean. Q. J. R. Meteorol. Soc. 141 (690), 1634–1645. http://dx.doi.org/10.1002/qj.2466.

Griffiths, J.F., Soliman, K.H., 1972. The northern desert (Sahara). World Surv. Climatol. Clim. Africa 10, 75–132.

Hannachi, A., Awad, A., Ammar, K., 2011. Climatology and classification of Spring Saharan cyclone tracks. Clim. Dynam. 37 (3), 473–491. http://dx.doi.org/10.1007/s00382-010-0941-9.

Harada, C., Sumi, A., Ohmori, H., 2003. Seasonal and year-to-year variations of rainfall in the Sahara desert region based on TRMM PR data. Geophys. Res. Lett. 30 (6), http://dx.doi.org/10.1029/2002GL016695.

Harris, I., Osborn, T.J., Jones, P., Lister, D., 2020. Version 4 of the CRU TS monthly high-resolution gridded multivariate climate dataset. Sci. Data 7 (1), 1–18. http://dx.doi.org/10.1038/s41597-020-0453-3.

Heistermann, M., Jacobi, S., Pfaff, T., 2013. Technical note: An open source library for processing weather radar data (wradlib). Hydrol. Earth Syst. Sci. 17 (2), 863–871. http://dx.doi.org/10.5194/hess-17-863-2013.

Hersbach, H., Bell, B., Berrisford, P., Hirahara, S., Horányi, A., Muñoz-Sabater, J., Nicolas, J., Peubey, C., Radu, R., Schepers, D., Simmons, A., Soci, C., Abdalla, S., Abellan, X., Balsamo, G., Bechtold, P., Biavati, G., Bidlot, J., Bonavita, M., Chiara, G.D., Dahlgren, P., Dee, D., Diamantakis, M., Dragani, R., Flemming, J., Forbes, R., Fuentes, M., Geer, A., Haimberger, L., Healy, S., Hogan, R.J., Hólm, E., Janisková, M., Keeley, S., Laloyaux, P., Lopez, P., Lupu, C., Radnoti, G., de Rosnay, P., Rozum, I., Vamborg, F., Villaume, S., Thépaut, J.-N., 2020. The ERA5 global reanalysis. Q. J. R. Meteorol. Soc. 146, 1999–2049. http://dx.doi.org/10.1002/qj.3803.

Hou, A.Y., Kakar, R.K., Neeck, S., Azarbarzin, A.A., Kummerow, C.D., Kojima, M., Oki, R., Nakamura, K., Iguchi, T., 2014. The global precipitation measurement mission. Bull. Am. Meteorol. Soc. 95, 701–722. http://dx.doi.org/10.1175/BAMS-D-13-00164.1.

Huang, J., Li, Y., Fu, C., Chen, F., Fu, Q., Dai, A., Shinoda, M., Ma, Z., Guo, W., Li, Z., Zhang, L., Liu, Y., Yu, H., He, Y., Xie, Y., Guan, X., Ji, M., Lin, L., Wang, S., Yan, H., Wang, G., 2017. Dryland climate change: Recent progress and challenges. Rev. Geophys. 55, 719–778. http://dx.doi.org/10.1002/2016RG000550.

Huang, J., Yu, H., Guan, X., Wang, G., Guo, R., 2016. Accelerated dryland expansion under climate change. Nature Clim. Change 6 (2), 166–171. http://dx.doi.org/10.1038/nclimate2837.

Huffman, G.J., Bolvin, D.T., Braithwaite, D., Hsu, K.L., Joyce, R.J., Kidd, C., Nelkin, E.J., Sorooshian, S., Stocker, E.F., Tan, J., Wolff, D.B., Xie, P., 2020. Integrated multi-satellite retrievals for the global precipitation measurement (GPM) mission (IMERG). Adv. Global Change Res. 67, 343–353. http://dx.doi.org/10.1007/978-3-030-24568-9_19.

Huffman, G., Stocker, E., Bolvin, D., Nelkin, E., Tan, J., 2019. GPM IMERG final precipitation L3 half hourly 0.1 degree x 0.1 degree V06. http://dx.doi.org/10.5067/GPM/IMERG/3B-HH/06.

Hurley, J.V., Boos, W.R., 2015. A global climatology of monsoon low-pressure systems. Q. J. R. Meteorol. Soc. 141, 1049–1064. http://dx.doi.org/10.1002/qj.2447.

IMS, 2020. Summary of the 12-14.3.2020 Weather Event (in Hebrew). Tech. Rep., Bet Dagan, Israel, pp. 1–6, URL https://ims.gov.il/sites/default/files/2020-09/%D7%A1%D7%99%D7%9B%D7%95%D7%9D%20%D7%90%D7%99%D7%A8%D7%95%D7%A2%20%D7%9E%D7%96%D7%92%20%D7%94%D7%90%D7%95%D7%95%D7%99%D7%A8%2012%20%D7%A2%D7%93%2014%20%D7%91%D7%9E%D7%A8%D7%A5%202020_0.pdf.

IPCC, 2021. IPCC, 2021: Climate Change 2021: The Physical Science Basis. Cambridge University Press, Cambridge, United Kingdom and New York, NY, USA, p. 2391. http://dx.doi.org/10.1017/9781009157896,

IRIN-News, 2010. Hail storms, record rains. In: United Nations Office for the Coordination of Humanitarian Affairs, (OCHA). URL https://www.thenewhumanitarian.org/report/90046/west-africa-hail-storms-record-rains.

Islam, M.A., Yu, B., Cartwright, N., 2020. Assessment and comparison of five satellite precipitation products in Australia. J. Hydrol. 590 (April), 125474. http://dx.doi.org/10.1016/j.jhydrol.2020.125474.

Keil, C., Chabert, L., Nuissier, O., Raynaud, L., 2020. Dependence of predictability of precipitation in the northwestern Mediterranean coastal region on the strength of synoptic control. Atmos. Chem. Phys. 20 (24), 15851–15865. http://dx.doi.org/10.5194/acp-20-15851-2020.

Kelley, O.a., 2014. Where the least rainfall occurs in the Sahara Desert, the TRMM radar reveals a different pattern of rainfall each season. J. Clim. 27 (18), 6919–6939. http://dx.doi.org/10.1175/JCLI-D-14-00145.1.

Kelso, N.V., Patterson, T., 2010. Introducing natural earth data - Naturalearthdata.Com. Geographia Tech., Special Issue 82–89.

Kidd, C., Becker, A., Huffman, G.J., Muller, C.L., Joe, P., Skofronick-Jackson, G., Kirschbaum, D.B., 2017. So, how much of the Earth's surface is covered by rain gauges? Bull. Am. Meteorol. Soc. 98 (1), 69–78. http://dx.doi.org/10.1175/BAMS-D-14-00283.1.

Kidd, C., Huffman, G., Maggioni, V., Chambon, P., Oki, R., 2021. The global satellite precipitation constellation current status and future requirements. Bull. Am. Meteorol. Soc. 102 (10), E1844–E1861. http://dx.doi.org/10.1175/BAMS-D-20-0299.1.

Knippertz, P., 2005. Tropical–Extratropical interactions associated with an atlantic tropical plume and subtropical jet streak. Mon. Weather Rev. 133 (9), 2759–2776. http://dx.doi.org/10.1175/MWR2999.1.

Knippertz, P., Fink, A.H., Reiner, A., Speth, P., 2003. Three late summer/early autumn cases of tropical-extratropical interactions causing precipitation in Northwest Africa. Mon. Weather Rev. 131 (1), 116–135. http://dx.doi.org/10.1175/1520-0493(2003)131<0116:TLSEAC>2.0.CO;2.

Krichak, S.O., Alpert, P., Krishnamurti, T.N., 1997. Interaction of topography and tropospheric flow - A possible generator for the Red Sea Trough? Meteorol. Atmos. Phys. 63 (3–4), 149–158. http://dx.doi.org/10.1007/BF01027381.

Lalaurette, F., 2003. Early detection of abnormal weather conditions using a probabilistic extreme forecast index. Q. J. R. Meteorol. Soc. 129 (594), 3037–3057. http://dx.doi.org/10.1256/qj.02.152.

Lavaysse, C., Flamant, C., Janicot, S., 2010. Regional-scale convection patterns during strong and weak phases of the Saharan heat low. Atmos. Sci. Lett. 11 (4), 255–264. http://dx.doi.org/10.1002/asl.284.

Lavaysse, C., Flamant, C., Janicot, S., Parker, D.J., Lafore, J.P., Sultan, B., Pelon, J., 2009. Seasonal evolution of the West African heat low: A climatological perspective. Clim. Dynam. 33 (2–3), 313–330. http://dx.doi.org/10.1007/s00382-009-0553-4.

Lejeune-Kaba, F., 2010.

Li, R., Guilloteau, C., Kirstetter, P.E., Foufoula-Georgiou, E., 2023. How well does the IMERG satellite precipitation product capture the timing of precipitation events? J. Hydrol. 620 (PB), 129563. http://dx.doi.org/10.1016/j.jhydrol.2023.129563.

Li, Z., Tang, G., Hong, Z., Chen, M., Gao, S., Kirstetter, P., Gourley, J.J., Wen, Y., Yami, T., Nabih, S., Hong, Y., 2021. Two-decades of GPM IMERG early and final run products intercomparison: Similarity and difference in climatology, rates, and extremes. J. Hydrol. 125975. http://dx.doi.org/10.1016/j.jhydrol.2021.125975.

Lickley, M., Solomon, S., 2018. Drivers, timing and some impacts of global aridity change. Environ. Res. Lett. 13, http://dx.doi.org/10.1088/1748-9326/aae013.

Mabbutt, J.A., 1977. Desert Landforms, Second pri The MIT Press, Cambridge, Massachusetts, USA, p. 340.

Maddox, R.A., Canova, F., Hoxit, R.L., 1980. Meteorological characteristics of flash floods events over the Western United States. Mon. Wather Rev. 108, 1866–1877.

Mahmoud, M.T., Mohammed, S.A., Hamouda, M.A., Mohamed, M.M., 2021. Impact of topography and rainfall intensity on the accuracy of imerg precipitation estimates in an arid region. Remote Sens. 13 (1), 1–17. http://dx.doi.org/10.3390/rs13010013.

Marra, F., Armon, M., Morin, E., 2022a. Coastal and orographic effects on extreme precipitation revealed by weather radar observations. Hydrol. Earth Syst. Sci. 26 (5), 1439–1458. http://dx.doi.org/10.5194/hess-26-1439-2022.

Marra, F., Borga, M., Morin, E., 2020. A unified framework for extreme subdaily precipitation frequency analyses based on ordinary events. Geophys. Res. Lett. 47, 1–8. http://dx.doi.org/10.1029/2020GL090209.

Marra, F., Levizzani, V., Cattani, E., 2022b. Changes in extreme daily precipitation over Africa: Insights from a non-asymptotic statistical approach. J. Hydrol. X 16, http://dx.doi.org/10.1016/j.hydroa.2022.100130.

Marra, F., Morin, E., Peleg, N., Mei, Y., Anagnostou, E.N., 2017. Intensity–duration–frequency curves from remote sensing rainfall estimates: Comparing satellite and weather radar over the eastern Mediterranean. Hydrol. Earth Syst. Sci. 21 (5), 2389–2404. http://dx.doi.org/10.5194/hess-21-2389-2017.

Marra, F., Zoccatelli, D., Armon, M., Morin, E., 2019. A simplified MEV formulation to model extremes emerging from multiple nonstationary underlying processes. Adv. Water Resour. 127, 280–290. http://dx.doi.org/10.1016/j.advwatres.2019.04.002.

Mekawy, M., Saber, M., Mekhaimar, S.A., Zakey, A.S., Robaa, S.M., Abdel Wahab, M., 2023. Evaluation of WRF microphysics schemes performance forced by reanalysis and satellite-based precipitation datasets for early warning system of extreme storms in hyper arid environment. Climate 11 (1), http://dx.doi.org/10.3390/cli11010008.

Mekonnen, A., Thorncroft, C.D., Aiyyer, A.R., 2006. Analysis of convection and its association with African easterly waves. J. Clim. 19 (20), 5405–5421. http://dx.doi.org/10.1175/JCLI3920.1.

Menne, M.J., Durre, I., Vose, R.S., Gleason, B.E., Houston, T.G., 2012. An overview of the global historical climatology network-daily database. J. Atmos. Ocean. Technol. 29 (7), 897–910. http://dx.doi.org/10.1175/JTECH-D-11-00103.1.

Milewski, A., Elkadiri, R., Durham, M., 2015. Assessment and comparison of TMPA satellite precipitation products in varying climatic and topographic regimes in Morocco. Remote Sens. 7 (5), 5697–5717. http://dx.doi.org/10.3390/rs70505697.

Milewski, A., Sultan, M., Yan, E., Becker, R., Abdeldayem, A., Soliman, F., Gelil, K.A., 2009. A remote sensing solution for estimating runoff and recharge in arid environments. J. Hydrol. 373 (1–2), 1–14. http://dx.doi.org/10.1016/j.jhydrol.2009.04.002.

Mirzabaev, A., Wu, J., Evans, J., Garcia-Oliva, F., Hussein, I.A.G., Iqbal, M.H., Kimutai, J., Knowles, T., Meza, F., Nedjroaoui, D., Tena, F., Türke, M., Vázquez, R.J., Weltz, M., 2019. Desertification. In: Shukla, P.R., Skeg, J., Buendia, E.C., Masson-Delmotte, V., Pörtner, H.-O., Roberts, D.C., Zhai, P., Slade, R., Connors, S., van Diemen, S., Ferrat, M., Haughey, E., Luz, S., Pathak, M., Petzold, J., Pereira, J.P., Vyas, P., Huntley, E., Kissick, K., Belkacemi, M., Malley, J. (Eds.), Climate Change and Land: An IPCC Special Report on Climate Change, Desertification, Land Degradation, Sustainable Land Management, Food Security, and Greenhouse Gas Fluxes in Terrestrial Ecosystems. http://dx.doi.org/10.1017/9781009157988.005.

badawy Moawad, M., omar Abdel aziz, A., Mamtimin, B., 2016. Flash floods in the Sahara: A case study for the 28 January 2013 flood in Qena, Egypt. Geomatics, Nat. Hazards Risk 7 (1), 215–236. http://dx.doi.org/10.1080/19475705.2014.885467.

Mohr, S., Ehret, U., Kunz, M., Ludwig, P., Caldas-Alvarez, A., Daniell, J.E., Ehmele, F., Feldmann, H., Franca, M.J., Gattke, C., Hundhausen, M., Knippertz, P., Küpfer, K., Mühr, B., Pinto, J.G., Quinting, J., Schäfer, A.M., Scheibel, M., Seidel, F., Wisotzky, C., 2023. A multi-disciplinary analysis of the exceptional flood event of July 2021 in central Europe - Part 1: Event description and analysis. Nat. Hazards Earth Syst. Sci. 23 (2), 525–551. http://dx.doi.org/10.5194/nhess-23-525-2023.

Morin, E., Marra, F., Armon, M., 2020. Dryland precipitation climatology from satellite observations. In: Levizzani, V., Kidd, C., Kirschbaum, D., Kummerow, C., Turk, F.J. (Eds.), Satellite Precipitation Measurement, second ed. Springer Nature Switzerland, pp. 843–859. http://dx.doi.org/10.1007/978-3-030-35798-6_19.

Morsy, M., Scholten, T., Michaelides, S., Borg, E., Sherief, Y., Dietrich, P., 2021. Comparative analysis of TMPA and IMERG precipitation datasets in the arid environment of El-Qaa Plain, Sinai. Remote Sens. 13 (4), 588. http://dx.doi.org/10.3390/rs13040588.

Nicholson, S.E., 2009. A revised picture of the structure of the "monsoon" and land ITCZ over West Africa. Clim. Dynam. 32 (7–8), 1155–1171. http://dx.doi.org/10.1007/s00382-008-0514-3.

Nicholson, S.E., 2011. Dryland Climatology. Cambridge University Press, New York, p. 516. http://dx.doi.org/10.1017/CBO9780511973840.

Nicholson, S.E., 2018. Climate of the Sahel and West Africa. In: Oxford Research Encyclopedia of Climate Science, (no. September 2018), pp. 1–47. http://dx.doi.org/10.1093/acrefore/9780190228620.013.510.

OCHA, 2023. Libya: Flood response; Humanitarian update as of 17 October 2023 (october). URL https://reliefweb.int/report/libya/libya-flood-response-humanitarian-update-17-october-2023-enar.

OECD, 2014. An Atlas of the Sahara-Sahel. West African Studies, OECD, p. 256. http://dx.doi.org/10.1787/9789264222359-en.

Otterman, J., Sharon, D., 1979. Day-night partitioning of rain in an arid region. Computational approaches, results for the Negev and meteorological-climatological implications. J. de Recherches Atmos. 13 (1), 11–20.

Parker, D.J., Burton, R.R., Diongue-Niang, A., Ellis, R.J., Felton, M., Taylor, C.M., Thorncroft, C.D., Bessemoulin, P., Tompkins, A.M., 2005. The diurnal cycle of the West African monsoon circulation. Q. J. R. Meteorol. Soc. 131 (611), 2839–2860. http://dx.doi.org/10.1256/qj.04.52.

Pedgley, D.E., 1974. an exceptional desert rainstorm At Kufra, Libya. Weather 29 (2), 64–71. http://dx.doi.org/10.1002/j.1477-8696.1974.tb04340.x.

Peleg, N., Marra, F., Fatichi, S., Molnar, P., Morin, E., Sharma, A., Burlando, P., 2018. Intensification of convective rain cells at warmer temperatures observed from high-resolution weather radar data. J. Hydrometeorol. JHM–D–17–0158.1. http://dx.doi.org/10.1175/JHM-D-17-0158.1.

Pfahl, S., Wernli, H., 2012. Quantifying the relevance of cyclones for precipitation extremes. J. Clim. 25 (19), 6770–6780. http://dx.doi.org/10.1175/JCLI-D-11-00705.1.

Pook, M.J., Risbey, J.S., Ummenhofer, C.C., Briggs, P.R., Cohen, T.J., 2014. A synoptic climatology of heavy rain events in the Lake Eyre and Lake Frome catchments. Front. Environ. Sci. 2 (NOV), 1–8. http://dx.doi.org/10.3389/fenvs.2014.00054.

Prein, A.F., Langhans, W., Fosser, G., Ferrone, A., Ban, N., Goergen, K., Keller, M., Tölle, M., Gutjahr, O., Feser, F., Brisson, E., Kollet, S., Schmidli, J., Van Lipzig, N.P., Leung, R., 2015. A review on regional convection-permitting climate modeling: Demonstrations, prospects, and challenges. Rev. Geophys. 53 (2), 323–361. http://dx.doi.org/10.1002/2014RG000475.

Rachdane, M., El Khalki, E.M., Saidi, M.E., Nehmadou, M., Ahbari, A., Tramblay, Y., 2022. Comparison of high-resolution satellite precipitation products in Sub-Saharan Morocco. Water 14 (20), http://dx.doi.org/10.3390/w14203336.

RFI, 2010. Nearly 30,000 made homeless by floods in east Burkina Faso. URL https://www.rfi.fr/en/africa/20100725-nearly-30000-made-homeless-floods-east-burkina-faso.

Rieder, J., 2023. Analysis of Meteorological Systems and Moisture Sources Leading to Lake-Filling Episodes in the Northwestern Sahara (Ph.D. thesis). ETH Zurich, p. 97. http://dx.doi.org/10.3929/ethz-b-000616946.

Rinat, Y., Marra, F., Armon, M., Metzger, A., Levi, Y., Khain, P., Vadislavsky, E., Rosensaft, M., Morin, E., 2021. Hydrometeorological analysis and forecasting of a 3-d flash-flood-triggering desert rainstorm. Nat. Hazards Earth Syst. Sci. 21 (3), 917–939. http://dx.doi.org/10.5194/nhess-21-917-2021.

Rodwell, M.J., Hoskins, B.J., 1996. Monsoons and the dynamics of deserts. Q. J. R. Meteorol. Soc. 122 (534), 1385–1404. http://dx.doi.org/10.1002/qj.49712253408.

Rodwell, M.J., Hoskins, B.J., 2001. Subtropical anticyclones and summer monsoons. J. Clim. 14, 3192–3211. http://dx.doi.org/10.1175/1520-0442(2001)014<3192:SAASM>2.0.CO;2.

Rubin, S., Ziv, B., Paldor, N., 2007. Tropical plumes over eastern North Africa as a source of rain in the Middle East. Mon. Weather Rev. 135 (12), 4135–4148. http://dx.doi.org/10.1175/2007MWR1919.1.

Russo, A., Sousa, P.M., Durão, R.M., Ramos, A.M., Salvador, P., Linares, C., Díaz, J., Trigo, R.M., 2020. Saharan dust intrusions in the Iberian Peninsula: Predominant synoptic conditions. Sci. Total Environ. 717, 137041. http://dx.doi.org/10.1016/j.scitotenv.2020.137041.

Saidi, M.E.M., Saouabe, T., El Fels, A.E.A., Khalki, E.M.E., Hadri, A., 2020. Hydro-meteorological characteristics and occurrence probability of extreme flood events in moroccan high atlas. J. Water Clim. Change 11 (1S), 310–321. http://dx.doi.org/10.2166/wcc.2020.069.

Saltikoff, E., Friedrich, K., Soderholm, J., Lengfeld, K., Nelson, B., Becker, A., Hollmann, R., Urban, B., Heistermann, M., Tassone, C., 2019. An overview of using weather radar for climatological studies successes, challenges, and potential. Bull. Am. Meteorol. Soc. 100 (9), 1739–1751. http://dx.doi.org/10.1175/BAMS-D-18-0166.1.

Schepanski, K., Heinold, B., Tegen, I., 2017. Harmattan, Saharan heat low, and West African monsoon circulation: Modulations on the Saharan dust outflow towards the North Atlantic. Atmos. Chem. Phys. 17 (17), 10223–10243. http://dx.doi.org/10.5194/acp-17-10223-2017.

Schepanski, K., Knippertz, P., 2011. Soudano-Saharan depressions and their importance for precipitation and dust: A new perspective on a classical synoptic concept. Q. J. R. Meteorol. Soc. 137 (659), 1431–1445. http://dx.doi.org/10.1002/qj.850.

Schepanski, K., Wright, T.J., Knippertz, P., 2012. Evidence for flash floods over deserts from loss of coherence in InSAR imagery. J. Geophys. Res.: Atmos. 117 (20), 1–10. http://dx.doi.org/10.1029/2012JD017580.

Scherrmann, A., Wernli, H., Flaounas, E., 2023. Origin of low-tropospheric potential vorticity in Mediterranean cyclones. Weather Clim. Dyn. 4 (1), 157–173. http://dx.doi.org/10.5194/wcd-4-157-2023.

Sharon, D., 1972. The spottiness of rainfall in a desert area. J. Hydrol. 17 (3), 161–175. http://dx.doi.org/10.1016/0022-1694(72)90002-9.

Shmilovitz, Y., Morin, E., Rinat, Y., Haviv, I., Carmi, G., Mushkin, A., Enzel, Y., 2020. Linking frequency of rainstorms, runoff generation and sediment transport across hyperarid talus-pediment slopes. Earth Surf. Processes Landforms n/a, http://dx.doi.org/10.1002/esp.4836.

Siman-Tov, S., Marra, F., 2022. Antecedent rainfall as a critical factor for the triggering of short-lived debris flows in arid regions. Nat. Hazards Earth Syst. Sci. Discussions 2022, 1–22. http://dx.doi.org/10.5194/nhess-2022-184.

Skinner, C.B., Poulsen, C.J., 2016. The role of fall season tropical plumes in enhancing Saharan rainfall during the African Humid Period. Geophys. Res. Lett. 43 (1), 349–358. http://dx.doi.org/10.1002/2015GL066318.

Soltani, M., Hamelers, B., Mofidi, A., van der Hoeven, T., Staal, A., Dekker, S.C., Arnault, J., Laux, P., Kunstmann, H., Lanters, M., 2022. A 20-year satellite-reanalysis-based climatology of extreme precipitation characteristics over the Sinai Peninsula. Earth Syst. Dyn. Discussions 2022, 1–25. http://dx.doi.org/10.5194/esd-2022-10.

Sprenger, M., Fragkoulidis, G., Binder, H., Croci-Maspoli, M., Graf, P., Grams, C.M., Knippertz, P., Madonna, E., Schemm, S., Škerlak, B., Wernli, H., 2017. Global climatologies of Eulerian and Lagrangian flow features based on ERA-Interim. Bull. Am. Meteorol. Soc. 98 (8), 1739–1748. http://dx.doi.org/10.1175/BAMS-D-15-00299.1.

Sun, Y., Solomon, S., Dai, A., Portmann, R.W., 2006. How often does it rain? J. Clim. 19 (1996), 916–934. http://dx.doi.org/10.1175/JCLI3672.1.

Tabari, H., 2021. Extreme value analysis dilemma for climate change impact assessment on global flood and extreme precipitation. J. Hydrol. 593 (December 2020), 125932. http://dx.doi.org/10.1016/j.jhydrol.2020.125932.

Taylor, C.M., Parker, D.J., Kalthoff, N., Gaertner, M.A., Philippon, N., Bastin, S., Harris, P.P., Boone, A., Guichard, F., Agusti-Panareda, A., Baldi, M., Cerlini, P., Descroix, L., Douville, H., Flamant, C., Grandpeix, J.Y., Polcher, J., 2011. New perspectives on land-atmosphere feedbacks from the African monsoon multidisciplinary analysis. Atmos. Sci. Lett. 12 (1), 38–44. http://dx.doi.org/10.1002/asl.336.

Tooth, S., 2000. Process, form and change in dryland rivers: A review of recent research. Earth Sci. Rev. 51 (1–4), 67–107. http://dx.doi.org/10.1016/S0012-8252(00)00014-3.

Tubi, A., Dayan, U., Lensky, I.M., 2017. Moisture transport by tropical plumes over the Middle East: A 30-year climatology. Q. J. R. Meteorol. Soc. 143 (709), 3165–3176. http://dx.doi.org/10.1002/qj.3170.

Tucker, C.J., Dregne, H.E., Newcomb, W.W., 1991. Expansion and contraction of the Sahara Desert from 1980 to 1990. Science 253 (5017), 299–301. http://dx.doi.org/10.1126/science.253.5017.299.

UNEP, 1992. World Atlas of Desertification. Edward Arnold, London, URL https://wedocs.unep.org/20.500.11822/42137.

UNHCR, 2010. Emergency assistance to victims of floods in Chad. URL https://www.unhcr.org/news/briefing/2010/8/4c653d419/emergency-assistance-victims-floods-chad.html.

Wang, X., Jiang, D., Lang, X., 2021. Future changes in aridity index at two and four degrees of global warming above preindustrial levels. Int. J. Climatol. 41, 278–294. http://dx.doi.org/10.1002/joc.6620.

Warner, T.T., 2004. Desert Meteorology. Cambridge University Press, New York, p. 595. http://dx.doi.org/10.1256/wea.201.04.

Wasko, C., Sharma, A., Westra, S., 2016. Reduced spatial extent of extreme storms at higher temperatures. Geophys. Res. Lett. 43 (8), 4026–4032. http://dx.doi.org/10.1002/2016GL068509.

Webster, P., Fasullo, J., 2003. MONSOON | dynamical theory. In: Encyclopedia of Atmospheric Sciences. pp. 1370–1386. http://dx.doi.org/10.1016/b0-12-227090-8/00236-0.

Wernli, H., Schwierz, C., 2006. Surface cyclones in the ERA-40 dataset (1958–2001). Part I: Novel identification method and global climatology. J. Atmos. Sci. 63 (10), 2486–2507. http://dx.doi.org/10.1175/JAS3766.1.

Yamazaki, A., Itoh, H., 2013. Vortex-vortex interactions for the maintenance of blocking. part I: The selective absorption mechanism and a case study. J. Atmos. Sci. 70 (3), 725–742. http://dx.doi.org/10.1175/JAS-D-11-0295.1.

Yin, J., Gao, Y., Chen, R., Yu, D., Wilby, R., Wright, N., Ge, Y., Bricker, J., Gong, H., Guan, M., 2023. Flash floods: Why are more of them devastating the world's driest regions? Nature 615 (7951), 212–215. http://dx.doi.org/10.1038/d41586-023-00626-9.

Ziv, B., Saaroni, H., Alpert, P., 2004. The factors governing the summer regime of the eastern Mediterranean. Int. J. Climatol. 24 (14), 1859–1871. http://dx.doi.org/10.1002/joc.1113.

Zoccatelli, D., Marra, F., Armon, M., Rinat, Y., Smith, J., Morin, E., 2019. Contrasting rainfall-runoff characteristics of floods in desert and mediterranean basins. Hydrol. Earth Syst. Sci. 23, http://dx.doi.org/10.5194/hess-23-2665-2019.

Zorzetto, E., Botter, G., Marani, M., 2016. On the emergence of rainfall extremes from ordinary events. Geophys. Res. Lett. 43, 8076–8082. http://dx.doi.org/10.1002/2016GL069445.